Published in final edited form as:
Nat Metab. 2022 June 01; 4(6): 739–758. doi:10.1038/s42255-022-00593-x.

Impaired oxygen-sensitive regulation of mitochondrial biogenesis within the von Hippel-Lindau syndrome

Shuijie Li[1,2,§], **Wenyu Li**[#1], **Juan Yuan**[#1], **Petra Bullova**[1], **Jieyu Wu**[1], **Xuepei Zhang**[3], **Yong Liu**[3], **Monika Plescher**[1], **Javier Rodriguez**[4], **Oscar C. Bedoya-Reina**[1], **Paulo R. Jannig**[5], **Paula Valente-Silva**[5], **Meng Yu**[6], **Marie Arsenian Henriksson**[1], **Roman A. Zubarev**[3], **Anna Smed-Sörensen**[6], **Carolyn K. Suzuki**[7], **Jorge L. Ruas**[5], **Johan Holmberg**[8], **Catharina Larsson**[9], **C. Christofer Juhlin**[9], **Alex von Kriegsheim**[4], **Yihai Cao**[1], **Susanne Schlisio**[1,§]

[1]Department of Microbiology, Tumor and Cell Biology, Karolinska Institutet, Stockholm, Sweden

[2]College of Pharmacy, Harbin Medical University, Harbin, 150081 China

[3]Department of Medical Biochemistry and Biophysics, Stockholm, Sweden

[4]Edinburgh Cancer Research Centre, IGMM, University of Edinburgh, Edinburgh, UK

[5]Department of Physiology and Pharmacology, Karolinska Institutet, Stockholm, Sweden

[6]Department of Medicine, Karolinska University Hospital, Stockholm; Sweden

[7]Department of Microbiology, Biochemistry and Molecular Genetics, New Jersey Medical School, Rutgers University, Newark, New Jersey 07103, USA

[8]Department of Molecular Biology, Faculty of Medicine, Umeå University, Umeå, Sweden

[9]Department of Oncology-Pathology, Karolinska Institutet, Karolinska University Hospital, SE-17176 Stockholm, Sweden

[#] These authors contributed equally to this work.

Abstract

Mitochondria are the main consumers of oxygen within the cell. How mitochondria sense oxygen levels remains unknown. Here we show an oxygen-sensitive regulation of TFAM, an activator of mitochondrial transcription and replication, whose alteration is linked to tumors arising in the von Hippel-Lindau syndrome. TFAM is hydroxylated by EGLN3 and subsequently bound by the tumor suppressor von Hippel-Lindau (pVHL). pVHL stabilizes

---

[§]Corresponding authors: Shuijie Li (shuijie.li@ki.se), Susanne Schlisio (susanne.schlisio@ki.se).

Reporting Summary.
Further information on research design is available in the Nature Research Reporting Summary linked to this article.

Author Contributions
Conceptualization, S.L. and S.S.; methodology, S.L., W.L., J.Y., P.B., J.W., M.P., Y.L., J.R., M.Y., P.R.J., P.V.-S., J.L.R., M.A.H. and A.v.K.; investigation, S.L., W.L., P.B., M.P., J.H., J.R., Y.C., A.v.K. and S.S.; computational investigation and analysis, O.C.B.-R. and X.Z.; PPGL sample collection and characterization, C.C.J. and C.L.; writing, S.L. and S.S.; funding acquisition, resources and supervision, S.S.

Competing Interests Statement
All authors declare they have no competing interests.

TFAM by preventing mitochondrial proteolysis. Cells lacking wild-type *VHL* or in which EGLN3 is inactivated have reduced mitochondrial mass. Tumorigenic *VHL* variants leading to different clinical manifestations fail to bind hydroxylated TFAM. In contrast, cells harboring the chuvash polycythemia $\mathrm{VHL}^{\mathrm{R200W}}$ mutation, involved in hypoxia-sensing disorders without tumor development, are capable of binding hydroxylated TFAM. Accordingly, VHL-related tumors, such as pheochromocytoma and renal cell carcinoma cells, display low mitochondrial content, suggesting that impaired mitochondrial biogenesis is linked to VHL tumorigenesis. Finally, inhibiting proteolysis by targeting LONP1 increases mitochondrial content in VHL-deficient cells and sensitizes therapy resistant tumors to sorafenib treatment. Our results offer pharmacological avenues to sensitize therapy-resistant VHL tumors by focusing on the mitochondria.

Hypoxia inducible transcription factor (HIFα) functions as a key regulator of cellular and systemic homeostatic response to hypoxia. The process orchestrating the oxygen-sensitive regulation of the HIFs is regulated by the oxygen-dependent activity of the prolyl hydroxylase enzymes (EGLN). Prolyl hydroxylation of HIFα allows substrate recognition by the von Hippel–Lindau tumor suppressor protein (pVHL) causing HIFα ubiquitination and degradation under normal oxygen concentrations [1–3]. Although mitochondria are the major consumers of oxygen in the cell, mitochondrial biogenesis has not been reported to be directly regulated by HIFα. However, HIF-1α has been reported to potentially inhibit mitochondrial biogenesis indirectly by repression of c-MYC activity [4].

Von Hippel-Lindau (VHL) disease is a hereditary cancer syndrome caused by mutations of the *VHL* gene resulting in different tumor subtypes including haemangioblastoma (HB) of the retina and the nervous system, clear cell renal carcinoma (ccRCC) and pheochromocytoma and paraganglioma (PPGL)[5]. HIF2α deregulation plays an important role in VHL-defective tumors, however, HIF2α mutations have only been observed in some sporadic cases of PPGL and have not been observed in ccRCC [6–8]. Moreover, the discovery of the oxygen-sensitive regulation of HIFα by pVHL cannot explain the mechanisms underlying the complex genotype–phenotype correlations in VHL syndrome. Type 1 VHL disease is defined as ccRCC and HB with low risk of PPGL and caused by truncating or missense *VHL* mutations. In contrast, Type 2 VHL disease is associated with *VHL* missense mutations and defined by PPGL, either alone (type 2C) or in combination with HB (type 2A) or with HB and ccRCCs (type 2B). Importantly, some germline type 2C *VHL* mutants in familial PPGL retain the ability to suppress HIFα [9,10]. Therefore, VHL's canonical substrate, HIFα, cannot fully explain the complex genotype-phenotype manifestation within the VHL syndrome and there is no evidence that HIFα deregulation is sufficient to cause cancer [11]. Instead, a number of other VHL functions independent of HIFα regulation have been ascribed to pVHL, including binding to fibronectin, collagen, atypical PKC, SFMBT1, TBK1, ZHX2 and AKT [12–19]. Previously, we also described a new VHL target, BIM-EL, that links type 2C *VHL* mutations to PPGL independent of HIFα regulation [20].

Another puzzling phenotype of *VHL* germline mutations has been described in patients from the Chuvash region that are homozygotes for the VHL^{R200W} mutation [21]. Whereas germline *VHL* mutations commonly predispose patients to the development of multiple tumors, homozygous carriers of germline VHL^{R200W} mutation show total absence of tumor development despite increased HIFα signaling [22–24]. These patients present with a congenital erythrocytosis (excess of red blood cell production) named Chuvash polycythemia [21]. The absence of tumor development in Chuvash polycythemia patients suggests that deregulation of HIFα may not be sufficient to drive tumorigenesis in the VHL cancer syndrome and that VHL has other substrates that are required for tumor suppression.

Here we identified an oxygen sensitive function of pVHL regulating mitochondrial biogenesis independent of the canonical substrate HIFα, that is defective in all VHL cancer syndrome mutations we tested, but normal in VHL^{R200W} Chuvash mutation. TFAM, a key activator of mitochondrial transcription and replication is hydroxylated by the oxygen-sensitive hydroxylase EGLN3 on proline 53/56 and subsequently bound and stabilized by pVHL. VHL related tumors such as PPGL and ccRCC show low mitochondrial content, implicating that lack of mitochondrial content is related to malignancies of tumorigenesis in the VHL syndrome.

Results

Mitochondrial content is regulated by pVHL

Germline type 2C *VHL* mutations predisposing to PPGL retain the ability to suppress HIFα [9,10]. To identify the pVHL functions independent of its canonical substrate HIFα, we performed comparative proteomics on of PPGL (n= 10) with wild-type or mutated *VHL* (Extended Data Fig.1a). The cellular proteomes from primary PPGL tumors were extracted and analyzed by nanoLC-MS/MS. 6,196 proteins were identified and quantified, 5,576 of which were common to all the samples (Supplementary Table S1). To investigate the effect of *VHL* mutations, we combined the proteome of all the *VHL* wild-type PPGL samples and compared it with the *VHL*-mutant proteome (Fig. 1a). We observed a significantly larger percentage of mitochondrial proteins downregulated in *VHL*-mutant samples as compared to wild-type PPGL samples (Fig. 1a,b and Extended Data Fig.1b, uncorrected *p*-value=7.95×10^{-35}, Fisher exact test). Among the significantly differentially expressed proteins, 36 of the top 50 (*e.g.* 72%) downregulated in *VHL* mutant PPGL were mitochondrial proteins including the mitochondrial-encoded protein MT-CO3 (Fig. 1c), implicating that mitochondrial proteomes differ between *VHL* mutant and wild-type PPGL. Furthermore, Gene Ontology terms enrichment was tested among the significantly top 50 up- and down-regulated proteins (Fig. 1d, $p<0.05$, two-tailed unpaired *t* test). Response to hypoxia and pyruvate metabolism were found as the most significantly enriched biological processes for the up-regulated proteins, while down-regulated proteins related to electron transport and mitochondrial part were over-represented in biological processes and cellular component according to FDR values in STRING results (Fig. 1d and Extended Data Fig.1c).

HIFα activation has been reported to be sufficient for many of the manifestations of *VHL* loss [1–3] and HIFα activation has also been reported to inhibit mitochondrial biogenesis [4]. To understand if the down-regulation of mitochondrial proteins in *VHL* mutant PPGL is HIFα dependent, we tested type 2C *VHL* mutants that predispose to PPGL without grossly deregulating HIFα [9]. Compared to wild-type *VHL*, the type 2C *VHL*-mutants (VHL^{L188V} and VHL^{R64P}) were clearly defective with respect to restoring abundance of mitochondrial proteins despite their ability to repress HIF2α (Fig. 1e). In particular, PGC-1α, a key transcriptional co-activator regulating mitochondrial biogenesis [25] was unaffected. To exclude potential effect of HIF2α regulating TFAM expression, we depleted *EPAS1* (HIF2α) in 786-O cells (Extended Data Fig.1e). *EPAS1* loss in *VHL*-WT or *VHL*-null cells had no effect on TFAM protein expression. Similarly to 786-O cells, wild-type *VHL* restored abundance of mitochondrial proteins in another ccRCC cell line A498 (Extended Data Fig.1d).

In addition, mitochondrial staining's of 786-O cells using mitotracker combined with flow cytometry analysis confirmed that mitochondrial fluorescent intensity was restored in *VHL* wild-type cells, but not in type 2C *VHL* mutant cells (Fig. 1f). Analyzing the proteome of *VHL*-null and VHL^{L188V} cells confirmed that the percentage of mitochondrial proteins was significantly lower in both VHL null cells (uncorrected p-value=4.51x $x10^{-44}$, Fisher exact test) as well as in type 2 *VHL* mutant cells (uncorrected p-value= 2.94x $x10^{-21}$, Fisher exact test) as compared to *VHL* wild-type expressing cells (Fig. 1g,h and Extended Data Fig.1h, i, Supplementary Table S2) Importantly, the majority of significant downregulated mitochondrial proteins in *VHL*-null cells (total of 656) was shared with the mitochondrial proteome in type 2C VHL^{L188V} cells (407 shared mitochondrial proteins) (Extended Data Fig.1f), suggesting a HIFα independent function of pVHL. Indeed, the percentage of significantly downregulated mitochondrial proteins that was shared between VHL^{L188V} and *VHL*-null cells was significantly higher than for significantly downregulated non-mitochondrial proteins (odds-ratio=1.26, uncorrected *p*-value = 0.0098, Fisher exact test). Additionally, the percentage of downregulated mitochondrial proteins shared between *VHL* mutated PPGL and VHL^{L188V} cells (Extended Data Fig.1g) was also significantly higher than for significantly downregulated non-mitochondrial proteins (odds-ratio=3.27, uncorrected *p*-value = $4.64x10^{-5}$, Fisher exact test), indicating HIFα independent function of pVHL.

Furthermore, it has been previously reported that primary ccRCC cells display minimal mitochondrial respiratory capacity and low mitochondrial number [26]. Thus we asked if other VHL type 1 (low risk PPGL), type 2A (low risk ccRCC) or type 2B (high risk ccRCC) mutants present similarly low mitochondrial contents as those observed in the type 2C *VHL* mutants. Only the reintroduction of wild-type *VHL* but none of the type 1, 2A, 2B or 2C mutations tested could restore the expression of mitochondrial proteins (Fig. 1i). In addition, we confirmed low mitochondrial content in a genetically defined system, using Cre-mediated deletion of *VHL* in MEFs homozygous for a floxed *VHL* allele (Fig. 1j, k).

Regulation of mitochondrial mass is hydroxylation dependent

pVHL has previously been shown to bind hydroxylated prolines of other substrates besides HIFα, such as AKT, BIM-EL, ZHX2, and pTBK1 [16,19,20,27]. To determine if regulation of mitochondrial content by pVHL is mediated by proline hydroxylation, we cultured 786-O cells expressing exogenous HA-VHL under anoxia (0.1% O_2) or with hydoxylase inhibitor dimethyloxaloylglycine (DMOG) and found that mitochondrial protein levels were decreased, similar to that of *VHL*-null cells under these conditions (Fig. 2a). To investigate the prolyl hydroxylase that may contribute to the regulation of mitochondrial proteins by pVHL, we silenced the three EGLN family members in HeLa and 786-O cells expressing

VHL and found that EGLN3 is the primary prolyl hydroxylase that showed the most robust decrease of mitochondrial proteins (Fig. 2b and Extended Data Fig. 2a, b). Consistent with these results, mito-tracker staining's of mitochondria and corresponding flow cytometry analysis confirmed significantly low mitochondrial content in *VHL* expressing cells in which *EGLN3* was downregulated with shRNA (Fig. 2c, d). To understand the impact of mitochondria content by loss of *EGLN3 in vivo*, we analyzed tissues from *EGLN3*-/- knockout (KO) mice. Mitochondrial proteins in *EGLN3-/-* mouse superior cervical ganglia (P1 SCG), adult adrenal medulla and cerebellum (P7) were remarkably reduced (Fig. 2e and Extended Data Fig. 2c). However, other tissues such as heart and skeletal muscle did not show any changes in mitochondrial protein content (Fig. 2f and Extended Data Fig. 2d). It is possible that degradation of mitochondrial proteins by mitochondrial protease LONP1 might contribute to these tissue-specific differences. Low LONP1 protein expression in skeletal muscle and heart is demonstrated in the human protein atlas (https://www.proteinatlas.org/ENSG00000196365-LONP1/tissue) and thus might contribute to higher mitochondrial content in these tissues independent of EGLN3 expression.

In addition, we detected decreased expression of mitochondrial proteins in *EGLN3*-/- mouse embryonic fibroblasts (MEFs) when cultured more than 5 passages (p5), but not in their first or second passage (Extended Data Fig.2e, f). Mito-Tracker staining visualizing mitochondria and corresponding flow cytometry analysis confirmed significant low mitochondrial content in *EGLN3*-/- MEFs cultured beyond 5 passages (Extended Data Fig.2g). Consistent with our observations in 786-O cells expressing wild-type pVHL (Fig. 2a), *EGLN3* wild-type MEFs (p5) showed low abundance of mitochondrial proteins when cultured under anoxia, or with hydroxylase inhibitors (Extended Data Fig.2h). To confirm that low mitochondrial content in *EGLN3-/-* Mefs (p5) is mediated by EGLN3 hydroxylase activity, we transduced cells with lentivirus encoding wild-type *EGLN3* (WT) or a catalytic-dead *EGLN3*-H196A mutant. Mitochondrial content was restored in *EGLN3-/-* MEFs transduced with Lenti-EGLN3-WT, but not Lenti-EGLN3-H196A mutant (Fig. 2g, h). Thus, EGLN3 hydroxylation activity regulates mitochondrial content under these conditions. Next, we asked whether changes in mitochondrial content observed in some tissues of *EGLN3* constitutive KO mice would culminate in an exercise intolerance phenotype, a common feature in settings of decreased mitochondrial biogenesis. Thus, we analyzed exercise endurance in younger and older *EGLN3* mice using a treadmill running test. We observed a minor, but significant impairment in exercise capacity in older *EGLN3-/-* males (56-60 weeks) (Fig. 2i), but not in younger males 18-19 weeks of age (Extended Data Fig.2i). Thus, the decreased mitochondrial content observed in certain tissues does not seem to have an impact in the exercise capacity of younger mice, but might play a more indirect role during aging.

TFAM hydroxylation on Proline 53/66 causes pVHL recognition

To understand the mechanism how pVHL can regulate mitochondrial content depending on EGLN3 hydroxylation activity, we investigated regulators of mitochondrial biogenesis, a process by which cells increase their individual mitochondrial mass and copy. Mitochondrial biogenesis is largely coordinated by PGC-1α [28] which in turn, regulates the activity of mitochondrial transcription factor A (TFAM), a key activator of mitochondrial transcription and mitochondrial genome replication [29]. pVHL and EGLN3 restored TFAM protein abundance in *VHL*-null cells (Fig. 1e, i and Fig. 3a) and in *EGLN3*-/- cells (Fig. 2g, h) respectively, whereas PGC1α protein abundance remained unaffected (Fig. 3a). Since TFAM is localized at the mitochondria, we performed mitochondrial fractionation and found that both, pVHL and EGLN3, partially localized to the mitochondria (Fig. 3b), consistent with previous reports [30]. Interestingly, VHL^{L188V} type 2C mutation was barely detected in the mitochondria fraction (Fig. 3b). To validate that pVHL and EGLN3 are localized within the mitochondria, we performed proteinase K digestion to exclude proteins at the mitochondria outer membrane. This allows to detect proteins within the inner membrane or matrix only (Fig. 3c and S3a). In *VHL* expressing 786-O cells, pVHL was detected in both cytosol, and also within the mitochondria post proteinase K digestion (Fig. 3c). In addition, we could also detect endogenous EGLN3 and endogenous pVHL within the mitochondria post proteinase K digestion (Extended Data Fig. 3a).

To investigate direct binding of pVHL with endogenous TFAM within the mitochondria in intact cells, we performed proximity ligation assays (PLA) combined with mitochondrial staining. We detected PLA fluorescent signal caused by endogenous TFAM binding to pVHL in *VHL* expressing 786-O cells, but not in *VHL*-null cells (Fig. 3d,e and S3b-d). We visualized PLA fluorescent signal with standard maximum intensity projection and further used spatial resolution with orthogonal view to the projection axis to validate mitochondrial localization (Fig. 3d,e and Extended Data Fig. 3b-d).

To further explore whether prolyl-hydroxylation of TFAM by EGLN3 is responsible for the pVHL-dependent regulation of TFAM abundance, we fist investigated if pVHL interacts with endogenous TFAM in 786-O cells expressing HA-VHL. TFAM was readily detected in anti-HA immunoprecipitates of cells expressing HA-VHL unless *EGLN3* (but not *EglN1* or *EglN2)* was downregulated with an effective shRNA (Fig. 3f). Furthermore, TFAM co-immunoprecipitated only with wild-type *VHL*, but not with VHL^{L188V} type 2C mutant (Fig. 3g). Moreover, when 786-O cells were treated with the protein synthesis inhibitor cycloheximide, the half-life of TFAM was shorter in *VHL*-/- cells compared to wild-type *VHL* expressing cells (Fig. 3h). Similarly, the half-life of TFAM was shorter in *EGLN3*-/- KO MEFs compared to wild-type MEFs (Fig. 3i), indicating that pVHL and EGLN3 stabilize TFAM protein.

To test whether prolyl-hydroxylation is responsible for the VHL-dependent regulation of TFAM protein abundance, we investigated if TFAM could be hydroxylated by EGLN3 and subsequently recognized by pVHL. *In vitro* translated full length TFAM-myc was Myc-immunoprecipitated and used in EGLN3 hydroxylation assays. TFAM-myc captured ^{35}S-labeled pVHL after incubation with EGLN3 wild-type, but not with catalytic-impaired EGLN3-H196A mutant (Fig. 4a). Furthermore, a pan-hydroxyproline antibody immunoprecipitated Flag-TFAM from 293 cells that exogenously expressed EGLN3 unless the EGLN3 was catalytically inactive or the cells were treated with DMOG (Fig. 4b). Hydroxyproline antibody immunoprecipitation of Flag-TFAM was not detected with exogenously expressed EGLN1 or EGLN2 (Extended Data Fig. 4a).

Recent reports demonstrated that phosphorylation within the HMG1 (high mobility group 1) domain of TFAM by protein kinase A (PKA) promotes its degradation by the mitochondrial

LONP1 protease [31,32]. Since we observed that EGLN3 is responsible for the pVHL-dependent TFAM stabilization, we generated a 40 aa peptide (TFAM 31-70) spanning the HMG1 domain containing the PKA phosphorylation sites (Fig. 4c) to identify potential hydroxylation residues. Proline hydroxylation was assayed by ^{35}S-VHL capture and confirmed by LC-MS/MS analysis (Fig. 4c-f). TFAM-peptide-31-70 captured ^{35}S-VHL after the EGLN3 hydroxylation reaction, but not after the hydroxylation reaction with EGLN3-H196A catalytic impaired mutant (Fig. 4d). This was a specific function of EGLN3 amongst the EGLN paralogs (Fig. 4d), consistent with our earlier observations that regulation of TFAM abundance (Fig. 2b and S2b) and hydroxyproline antibody immunoprecipitation of TFAM (Extended Data Fig. 4a) is a distinguishing feature of EGLN3. Hydroxylation of the TFAM-peptide-31-70 was confirmed by LC-MS/MS analysis (Fig. 4e, f and Extended Data Fig. 4b-f). MS confirmed that EGLN3 catalyzes the hydroxylation of proline 53 and proline 66 (Fig. 4e, f and Extended Data Fig. 4b, c). We detected mono-hydroxylated peptide on either proline 53 or proline 66 (Extended Data Fig. 4d, e). The detected intensity of each proline hydroxylated peptide was quantified and normalized to the non-hydroxylated peptide (Extended Data Fig. 4f). To understand the importance of mono- or potential di-hydroxylation of the respective proline residues for pVHL binding, we synthesized TFAM-peptide-31-70 peptides with the proline to alanine substitutions P50A, P53A, P66A, P53/66A, and measured their hydroxylation by EGLN3 using the ^{35}S-VHL capture assay (Fig. 4g). The P50A proline substitution did not alter hydroxylation relative to the wild-type peptide. In contrast, the P53A and P66A substitutions significantly impaired ^{35}S-VHL capture and the double substitutions P53/66A completely abolished ^{35}S-VHL recognition (Fig. 4g). In a reciprocal experiment, we synthesized TFAM-peptide-31-70 in which both prolines 53 and 66 (P-OH-53/66) were hydroxylated (Extended Data Fig. 4g). As expected, hydroxylated peptide could, similar to the hydroxylated HIF1α-peptide (556–575), capture ^{35}S-VHL (Fig. 4h). In contrast, non-hydroxylated TFAM peptide (naïve) did not capture ^{35}S-pVHL. Our finding that TFAM expression can be restored by wild-type *VHL*, but not type 2C *VHL* mutants (Fig.1e,i and Fig. 3a), suggested that the latter cannot recognize hydroxylated TFAM. Indeed, type 2C pVHL mutants bound to a hydroxylated HIF1α and HIF2α peptides, but failed to bind hydroxylated TFAM peptide (P-OH-53/66) (Fig. 4h, I). Type 1 and type 2A/B pVHL mutants also failed to recognize hydroxylated TFAM (Fig. 4h, i). Next, we tested pVHL^{R200W} Chuvash mutation in the ability to bind hydroxylated TFAM. *VHL*^{R200W} has been identified in homozygous carriers with a congenitalerythrocytosis (Chuvash polycythemia) but with a total absence of tumor development [22–24]. In contrast to the VHL-cancer-syndrome mutations, hydroxylated TFAM peptide captured ^{35}S-VHL^{R200W} mutant similar as ^{35}S-VHL wild-type (Fig. 4i). However, HIF1α-P-OH and HIF2α-P-OH peptides were both partially impaired to capture ^{35}S-VHL^{R200W} (Extended Data Fig. 4h), confirming previous reports of partial altered HIFα signaling in Chuvash patients [22–24,33]. Thus, type 1, 2A, 2B and 2C pVHL mutations tested all failed to bind hydroxylated TFAM, regardless of whether they have the ability to bind hydroxylated HIFα or not. In contrast, pVHL^{R200W} polycythemia-mutation bound hydroxylated TFAM similar as wild-type VHL. In addition, we noticed that the type 2A pVHL^{Y98H} mutant associated with low risk ccRCC behaved similar as pVHL^{R200W} Chuvash mutant being partially, but not fully impaired in HIF2α-P-OH peptide binding, reinforcing the role of HIF2α as oncogenic driver in ccRCC (Extended Data Fig. 4h).

Next, we complimented these studies by expressing wild-type or mutant HA-pVHL in 786-O cells and performing pulldown assays with immobilized TFAM or HIF2α peptides. As expected, wild-type HA-VHL and Chuvash HA-VHL^{R200W} mutant bound similarly to the di-hydroxy-TFAM peptide (P-OH-53/66), but not to any VHL syndrome mutants (Fig. 4j and Extended Data Fig. 4i), confirming our *in vitro* translated ^{35}S-VHL capture assay (Fig. 4i). In contrast to TFAM binding and consistent with ^{35}S-VHL capture assay (Fig. 4i), HA-VHL^{R200W} capture to hydroxylated HIF2α peptide was partially impaired (Fig. 4j).

In summary, we observed that all tested VHL syndrome mutations failed to recognize hydroxylated TFAM. In contrast, VHL Chuvash polycythemia mutant had similar binding affinity as wild-type VHL to hydroxylated TFAM, but was impaired in binding hydroxylated HIFα.

pVHL binding to hydroxylated TFAM protects from LONP1 degradation

We observed that the half-life of TFAM protein was shorter in *VHL*-/- or *EGLN3*-/- cells compared to *VHL* or *EGLN3* expressing cells, demonstrating that pVHL and EGLN3 stabilize TFAM protein (Fig. 3h,i). Recent reports demonstrated that phosphorylation of TFAM by PKA promotes its degradation by the mitochondrial LONP1 protease [31,32]. Thus, we hypothesized that binding of pVHL to hydroxy-P53/P66-TFAM masks S55/S56 phosphorylation and LONP1 recognition site and thus prevents degradation by LONP1. First, we used the LONP1 protease inhibitor bortezomib (BTZ) to determine if low TFAM abundance in *EGLN3*-/- primary MEFs and *VHL*-null 786-O cells was due to protease degradation. BTZ increased TFAM protein abundance in *EGLN3*-/- MEFs to the level of *EGLN3+/+* MEFs (Fig. 5a). Likewise, BTZ treatment of *VHL*-/- cells (786-O) restored TFAM levels (Fig. 5b), providing evidence that loss of either *EGLN3* or *VHL* accelerates TFAM degradation. In addition, we observed that exogenous expression of inducible TFAM-P53A/P66A mutant in HEK293 cells was robustly decreased compared to TFAM wild type (Fig. 5c). As shown earlier, TFAM P53A/P66A mutant peptide failed to capture S35-VHL (Fig. 4g). We predict that TFAM-P53A/P66A protein can no longer bind pVHL, and therefore can be targeted by PKA phosphorylation and rapid LONP1 degradation. Thus, we investigated further if PKA phosphorylation of hydroxylated TFAM peptide is impaired by VHL binding. Preincubation with GST-VHL prevented the hydroxylated TFAM peptide from PKA binding and phosphorylation (Fig. 5d). Consistent with these results, we observed that PKA activation using Forskolin in HA-VHL-WT expressing cells (786-O) decreased TFAM protein to a similar level as observed in *VHL* null cells (Fig. 5e). In a reciprocal experiment using the PKA inhibitor H89 in 786-O cells, we observed increased TFAM protein abundance in *VHL* null cells to a similar level as observed in HA-VHL-WT expressing cells (Fig. 5f).

Next, we set out to test the hypothesis that free TFAM (not bound to mtDNA) is resistant to LONP1 degradation when bound to VHL. Purified TFAM and LONP1 were incubated with ATP/Mg^{2+} causing TFAM being rapidly degraded (Fig. 5g). In contrast, when purified TFAM was hydroxylated by EGLN3 and subsequently incubated with purified GST-VHL prior to LONP1 incubation, TFAM became resistant to LONP1 degradation (Fig. 5g). Hydroxylation assay with catalytic dead EGLN3-H196A mutant however impaired GST-

VHL binding and TFAM was rapidly degraded by LONP1 despite incubation with GST-VHL.

Thus, we conclude that binding of pVHL to hydroxylated TFAM prevents TFAM from LONP1 recognition and degradation and thus allows free TFAM protein to stabilize in the absence of mtDNA binding.

LONP1 inhibition sensitizes VHL null ccRCC cells to sorafenib

The decrease of mitochondrial content observed in the *VHL* mutated PPGL and ccRCC cells (Fig. 1) suggests that mitochondrial content is a pathogenic target within the VHL cancer syndrome. Indeed, high expression of either catalytic subunit of PKA (PRKACA) or LONP1 that facilitates TFAM degradation were associated with shorter overall survival of ccRCC patients (Fig. 5h,i). Thus, we hypothesized that the decreased mitochondrial content in ccRCC might contribute to therapy resistance and contribute to lower overall survival in these patients. *VHL* null 786-O cells were resistant to apoptosis in contrast to *VHL* wild type expressing cells when treated with sorafenib (Fig. 5j,k). Sorafenib is a kinase inhibitor approved for the treatment of primary kidney cancer, advanced primary liver cancer, AML and advanced thyroid carcinoma. Indeed, *VHL* null cells pre-treated with LONP1 inhibitor bortezomib (BTZ) were re-sensitized to sorafenib and underwent complete apoptosis similar as *VHL* wild type expressing cells (Fig. 5j,k). This suggests that the low of mitochondrial content might contribute to therapy resistance.

To examine if *VHL*-null ccRCC can be re-sensitized to sorafenib treatment *in vivo*, we subcutaneously transplanted *VHL*-null 786-O cells into immunocompromised SCID mice. After approximately 4 weeks of tumor growth, mice were treated with either DMSO (control), sorafenib (15 mg/kg), bortezomib (1 mg/kg), or with combination of both, sorafenib and bortezomib. (Fig. 5l, m). Treatment with sorafenib or bortezomib alone did not significantly inhibit tumor growth compared with control treatment (Figure 5l, m). However, combination treatment with sorafenib and bortezomib resulted in significant inhibition of tumor growth compared with single or control treatment (Figure 5l, m), recapitulating our *in-vitro* cell culture observation (Figure 5 j,k). Immunofluorescent staining's confirmed that combination treatment resulted in increased TFAM and mitochondrial protein MTCO2 (Fig. 5n). Collectively, these results indicate that *VHL*-null ccRCC cells are sensitized to sorafenib when combined with LONP1 inhibitor bortezomib, leading to a profound tumor growth defect *in vivo* that was associated with increased levels of mitochondrial content.

VHL restores oxygen consumption independent of HIFα

We observed that mitochondrial mass can be restored by wildtype *VHL*, but not type 2C *VHL* mutants that are normal in regard to HIFα regulation (Fig. 1f). Thus, we tested if the restored mitochondrial content resulted in functional mitochondria and increased cellular oxygen consumption rate. Compared to 786-O *VHL*-null cells, overall respiration was significantly increased in 786-O cells stably expressing wildtype *VHL* (WT), but not in cells expressing type 2C *VHL* mutants (Fig. 6a, Suppl Extended Data Fig. 5a), indicating that *VHL* can restore mitochondrial function independent of HIFα regulation. Glycolysis and glycolytic capacity measured by extracellular acidification rate (ECAR) in VHL type 2C cells was however in between *VHL*-null and *VHL* wildtype cells, suggesting that activation of HIFα in *VHL*-null cells additionally contributes to increased glycolysis (Extended Data Fig. 6a).

Consistent with our findings that pVHL mediated regulation of mitochondrial mass is EGLN3 dependent (Fig. 2b-d), cellular respiration was impaired in *VHL* expressing 786-O cells upon inactivation of *EGLN3* by an effective shRNA (Fig. 6b and Extended Data Fig. 5b). Consistent with these observations, glycolysis was increased upon inactivation of *EGLN3* by shRNA (Extended Data Fig. 6b). Furthermore, oxygen consumption rate was impaired (Fig. 6c and Extended Data Fig. 5c) and glycolysis was increased (Extended Data Fig. 6c) in primary *EGLN3-/-* MEFs (passage 5) compared to control *EGLN3+/+* MEFs. This was dependent on EGLN3 enzymatic activity, since respiration was restored in *EGLN3-/-* MEFs that were transduced with wild-type *EGLN3* (lenti-EGLN3-WT), but not when transduced with catalytic inactive mutant (lenti-EGLN3-H196A) (Fig. 6d, Extended Data Fig. 5d and Extended Data Fig. 6d).

To test if the low mitochondrial content in *VHL*-null cells will result in a glycolytic dependency to maintain energy homeostasis, we performed glucose deprivation or glycolysis inhibition and measured ADP:ATP ratio, a central parameter of cellular energy metabolism (Fig 6e-p). 786-O cells expressing *VHL* wildtype were resistant to glucose deprivation induced cell death, compared to *VHL*-null cells or cells expressing *VHL* type 2C, 2B, 2A, or type 1 mutants (Fig. 6e and Extended Data Fig. 5e). Similar results were observed by inhibiting glycolysis using hexokinase inhibitor (3-Bromopyruvatic Acid) or Lactate dehydrogenase (LDH) inhibitor gossypol (Fig. 6f-g). Glycolytic dependency was similarly observed in *EGLN3* null cells (Extended Data Fig. 5f-h). Furthermore, an unbalanced ADP/ATP ratio was significant induced upon glucose deprivation or glycolysis inhibitors in *VHL*-null or type 2C mutant cells but not in *VHL* wild-type expressing cells, indicating a cellular response to energy crisis (Fig.6h-j). Since PKA inhibitor (H89) restored TFAM expression in *VHL*-null cells, we explored if PKA inhibition can restore resistance to glycolysis inhibition in *VHL*-null cells. Similar to *VHL* wild type expressing cells, *VHL*-null cells showed resistance to glucose deprivation and glycolysis inhibition when pretreated with PKA inhibitor, and ADP/ATP ratio was restored (Fig. 6k-p).

In summary, 786-O cells lacking *VHL* or expressing type 2C *VHL* mutants depend on glycolysis to obtain energy. Restoring wild-type *VHL* or pretreating cells with PKA inhibitor restores mitochondrial content and function and promotes metabolic reprogramming to oxidative phosphorylation and thus reverse vulnerability to glycolysis inhibition induced cell death.

Low mitochondrial content causes impaired differentiation

It has been recently demonstrated that metabolic reprogramming from aerobic glycolysis to oxidative phosphorylation is tightly coupled to differentiation, though the exact molecular basis underlying the transition is unknown [34,35]. Thus, we asked if type 2C *VHL* cancer mutations contributing to low mitochondrial content can impair differentiation in PCC PC12 cells. PC12 cells have been used as a model to study differentiation by nerve growth factor NGF [36]. PC12 cells resemble differentiated sympathetic neurons when grown under low-serum conditions in the presence of NGF [37] (Fig. 7a, b). Neurite outgrowth and the induction of neuron-specific class III beta-tubulin (Tuj1) was evident within 6 days of NGF culture condition. Differentiation was accompanied by induction of mitochondrial mass measured by mitotracker staining and induction of TFAM protein (Fig 7a, b). Next, we generated stable PC12 cells expressing either human HA-*VHL* wild-type or type 2C *VHL* mutants and subsequently transduced cells with an effective shRNA silencing endogenous rat *VHL* (Extended Data Fig. 7a). Control cells (shSCR) grown in the presence of NGF differentiated as excepted evident by neurite outgrowth and Tuj1 induction. However, cells transduced with an effective shRNA inactivating endogenous rat *VHL* (sh-rat *VHL*) failed to respond to NGF mediated differentiation (Fig. 7c). In contrast, cells with restored expression of human HA-*VHL* fully rescued the differentiation induced by NGF as evident by neurite outgrowth, Tuj1 induction and induction of mitochondrial content. In contrast, cells restored with HA-*VHL*-L188V type 2C mutant showed no differentiation associated phenotypic changes or induction of Tuj1 or mitochondrial content (Fig. 7c, Extended Data Fig. 7a). Similar to inactivation of *VHL*, inactivation of *TFAM* upon transduction with an effective shRNA, PC12 cell showed no characteristics of phenotypical changes associated to NGF induced differentiation (Fig. 7d, e), indicating that low mitochondrial content prevents neural differentiation induced by NGF.

Discussion

Functional mitochondria are essential for the cell energy metabolism of most tumor types. At the same time, mutations in genes impairing oxidative phosphorylation causing defects in mitochondrial energy metabolism have been reported for a restricted subset of tumors such as succinate dehydrogenase in hereditary PPGL, RCC and gastrointestinal stromal tumor [38], fumarate hydratase in hereditary leiomyomatosis and RCC [39] and isocitrate dehydrogenase 1 (*IDH1*) and *IDH2* in secondary glioblastomas and acute myeloid leukemia [40,41]. Here we observed that all tested *VHL* cancer syndrome mutations (type 1 and type 2A, 2B, 2C), but not the *VHL*$^{\mathrm{R200W}}$ Chuvash polycythemia mutation, are impaired in regulating TFAM abundance and contribute to decreased mitochondrial mass (summarized in schematic Fig. 8). Patients with *VHL*$^{\mathrm{R200W}}$ mutation causing Chuvash polycythemia are reported to show total absence of tumor development despite increased HIFα signaling [22–24]. Thus, alterations in mitochondrial biogenesis might have a role in initiating and/or sustaining the transformed state, independent of HIFα oncogenic functions. In this regard, we found that low mitochondrial content in pheochromocytoma cells (PC12) expressing type 2C *VHL* mutants prevented NGF induced differentiation. Type 2C *VHL* mutation were clearly defective in binding hydroxylated TFAM and failed to restore mitochondrial content, despite their ability to suppress HIFα. Impaired mitochondrial biogenesis caused by germline VHL syndrome mutations might impair differentiation of a progenitor cell during embryonic development, independent of HIFα. In this regard, in most affected *VHL* carriers, the disease displays an autosomal dominant pattern of inheritance [42,43]. This is in contrast with gain-of-function HIF2α mutations that are observed in only few sporadic cases of PPGL and have not been detected to date in ccRCC [6–8]. Although HIF2α is considered to be an oncogenic driver in *VHL* related ccRCC, familial gain-of-function HIF2α mutation have only been reported to be associated with familial erythrocytosis [44].

Similar as in *VHL*-Chuvash polycythemia, patients with familial gain-of-function HIF2α mutation had no history of RCC, PPGL, or central nervous system HB, the hallmarks of the VHL syndrome. This suggests additional pVHL tumor suppressor functions outside of HIFα regulation and implies that activation of HIFα might be necessary, but not sufficient for driving tumorigenesis in the VHL cancer syndrome (Fig. 8a). Furthermore, recent data show that *VHL* related ccRCC can be classified into HIF2α dependent and independent tumors and that these tumors differ in HIF-2α levels and in their gene expression [45]. These observations also point to HIF independent mechanisms of tumorigenesis downstream of pVHL and thus may underlie differences in responsiveness to HIF2α inhibitor [45].

That non-cancerous *VHL*^{R200W} Chuvash polycythemia mutation was normal in regard of TFAM regulation in contrast to all other *VHL* syndromic cancer mutations, suggests that impaired mitochondrial biogenesis is an important feature of the VHL syndrome (schematic shown in Fig. 8a). Low mitochondrial content could provide an energetic vulnerability for all tumor types arising in the VHL syndrome, including type 2C PPGL. In this regard, we observed that *VHL*-null ccRCC cells or cells expressing type-2C *VHL* mutations are highly dependent upon glycolysis to maintain energy homeostasis and undergo rapid cell death when treated with glycolysis inhibitors. Efforts to target glucose uptake or lactate production however has been limited due to toxicity associated with hypoglycemia symptoms [46].

Advanced ccRCC is a lethal disease with a 5-year survival of only 11.7% [47] and traditional chemotherapy and radiation therapy are largely ineffective. We hypothesized that the low mitochondrial content in ccRCC might contribute to the known therapy resistance in ccRCC. *VHL*-null 786-O cells were resistant to apoptosis in contrast to *VHL* wild-type expressing cells when treated with sorafenib, a multi-kinase inhibitor approved for the treatment of primary kidney cancer. By understanding the precise molecular mechanism by which pVHL regulates mitochondrial mass, we performed pharmacological studies to increase mitochondrial content in *VHL*-deficient ccRCC cells. pVHL binding to hydroxylated TFAM, a key activator of mitochondrial transcription and replication, stabilizes TFAM by preventing LONP1 recognition and subsequent mitochondrial proteolysis (summarized in schematic Fig. 8b). *VHL*-null ccRCC cells responded to LONP1 inhibitor bortezomib, causing increase of mitochondrial content and re-sensitized cells to sorafenib. Combined treatment of both, sorafenib and bortezomib, provided a profound tumor growth defect *in vivo*. Thus, LONP1 inhibition provides a pharmacological tool to increase mitochondrial content in *VHL* deficient ccRCC and can sensitize therapy resistant ccRCC cells to sorafenib.

Methods

Cell culture

Human renal carcinoma cell line 786-O (ATCC, CRL-1932) and A498 (ATCC, HTB-44), HeLa cells (ATCC, CCL-2), 293FT cell line (ThermoFisher, R70007) and mouse embryonic fibroblasts (MEFs) were cultured in DMEM (glucose 4,5 g/L) containing 10% fetal bovine serum (FBS) in 5% CO_2 at 37 °C. *VHLfl/fl* and *EGLN3*-/- primary MEFs have been described [48] and isolation of primary MEFs has been described previously [49]. 786-O cells were purchased from the American Tissue Culture Collection. Rat PC12 cells (ATCC

CRL-1721) were differentiated with 50 ng/ml nerve growth factor in DMEM medium (glucose 1g/L) supplemented with 1% horse serum. Prior to differentiation, stable polyclonal PC12 cells expressing the indicated human *VHL* (hu*VHL*) species were selected with G418 (0.5 mg/mL) for 2 weeks. PC12 clones were transduced for 48 h with lentivirus encoding shRNA targeting endogenous rat *VHL* (endg. sh-rat*VHL*) or scramble control (shSCR) and subsequently treated with NGF for 6 days.

EGLN3 knockout mice

Generation of the *EGLN3* mouse strain (C57BL/6) has been previously described [48]. Animal experiments were performed in accordance with Swedish animal welfare laws authorized by the Stockholm Animal Ethics Committee (Dnr 7694/17). P1 Super cervical ganglia dissections of *EGLN3* pups are described in [50]. Mice were housed in IVCs (individually ventilated cages) with free access to food and water in constant temperature (20 ± 3 °C) and humidity (50 ± 10%). Light/dark cycle is in 12h:12h from 06.00 to 18.00 and 12 h darkness with dusk and dawn periods in between. The mice received standard diet from Special Diets Services CRM (P) 9.5mm pelleted (product code: 801722).

Human tissue specimens

Tumor tissue samples (PCC n=9 and PGL n=1) were collected from patients at the Karolinska University Hospital, Stockholm, Sweden, and previously characterized for mutations in PPGL susceptibility genes [51] (Supplementary Extended Data Fig.2). All samples were obtained with informed patient consent and with approval from the local ethical committees. *VHL* mutations in cases 21, 25, 96 and 108 as well as WT *VHL* status for the other 6 cases have been previously described [51].

Confocal microscopy

786-O and MEFs cells were cultured on glass coverslips and stained with MitoTracker Red CMXRos (100 nM) at 37 °C for 30 min, washed twice with pre-warmed phosphate-buffered saline (PBS), and fixed for 15 min in pre-warmed 4% paraformaldehyde. Coverslips were immersed into PBS overnight, and mounted using ProLong Diamond Antifade Mountant with DAPI (ThermoFisher, cat no: P36962). Fluorescence images were acquired using a Zeiss LSM 700 laser scanning confocal microscope equipped with a 63× Plan-Apochromat/1.4 NA Oil with DIC capability objective. The excitation wavelengths for MitoTracker Red CMXRos and DAPI were 579 nm and 405 nm, respectively. Images were acquired under the settings: frame size 1024, scan speed 6, and 12-bit acquisition and line averaging mode 8. Pinholes were adjusted so that each channel had the same optical slice of 1-1.2 μm.

Flow cytometry analysis

786-O or MEFs cells were stained with MitoTracker® Green FM (100 nM) at 37 °C for 30 min for labelling mitochondria. Mean fluorescence intensity (MFI) analysis of labelled mitochondria was performed by gating on single cells (FACS gating strategies are shown in Supplementary Information Fig.1). Samples were analysed on an LSRFortessa flow cytometer (BD Biosciences) and analysed using FlowJo software (Tree Star). Cell apoptosis rate was detected by Annexin V-FITC/PI staining. After 48 hours of treatment, the 786-O cell were rinsed by PBS and collected for Annexin V-FITC/PI staining. Each cell pellet was resuspended in 500 μL of binding buffer supplemented with 5 μL of FITC and 5 μL of PI, and the cells were incubated for 15 minutes. The apoptotic ratios were determined by flow cytometry.

Graded treadmill running test

All treadmill running experiments were approved by the regional animal ethics committee of Northern Stockholm, Sweden (#4039-2018 and #4359-2020) and mice were housed as described above. 58-60 weeks old aged male mice (wild type n=15, KO n=16) and young males 18-19 weeks old (wild type n=16 and KO n=16) were used. Acclimation to treadmill was performed with male wildtype and *EGLN3-/-* mice of the indicated age for 3 days prior to experiment by running 10 min per day. Each day, mice started with 5 min at a speed of 6 meter/min. On day 1, this was followed by 5 min at 9 m/min. On day 2, this was followed by 2 min at 9 m/min, 2 min at 12 m/min and 1 min at 6 m/min. On day 3, this was followed by 2 min at 9 m/min, 2 min at 15 m/min and 1 min at 6 m/min. The graded treadmill running test was performed on a 10° slope. During the test, the speed was increased every 3 minutes up to a maximum of 35 m/min. Exhaustion time was determined when the animal could no longer continue running despite of gentle prodding. Body weight was recorded after exhaustion in order to calculate work and power.

Mouse tumor models and treatment

Mouse tumor xenograft models were approved by the Swedish Board of Agriculture (ethical number 6197-2019). 6 – 8 weeks old male CB17/Icr-Prkdcscid/Rj mice were purchased from Janvier Labs (France). Mice were housed in IVCs (individually ventilated cages) with free access to food and water in constant temperature (20 ± 3 °C) and humidity (50 ± 10%). Light/dark cycle is in 12h:12h from 06.00 to 18.00 and 12 h darkness with dusk and dawn periods in between. The mice received standard diet from Special Diets Services CRM (P) 9.5mm pelleted (product code: 801722). They were randomly divided to each group. Approximately 5×10^6 786-O tumor cells were subcutaneously injected into the back along the mid dorsal line of each mouse. Tumor volume was measured every three days and calculated according to the standard formula (length × width2 ×0.52). Drug treatment was initiated when tumor volume reached to 5 mm3. 1% DMSO (Cat. STBJ9836, SIGMA) and sorafenib (15 mg/kg, Cat. SML2653, SIGMA) orally delivered to mice every day. BTZ (1 mg/kg, Cat. 3514175, MERCK) was intraperitoneally injected twice per week in either monotherapy or combination therapy. Experiment terminated when the tumor volume of 1% DMSO group reached to 1.2-1.3 cm3. The maximal tumor size permitted by the ethics committee was $2.5cm^3$ and the tumor size did not exceed the permitted tumor size.

Histology and immunofluorescence

Paraffin-embedded tissues were cut into 5 μm slides. Slides were baked for 1 h at 60 °C and deparaffinized in Tissue-clear (Cat. 1466, Sakura), and sequentially rehydrated in 99 %, 95 % and 70 % ethanol and counterstained with Haematoxylin and Eosin. Mounting was performed with PERTEX (Cat. 0081, HistoLab). Deparaffinized slides were boiling for 20 min in an unmasking solution (H3300, VECTOR) then subsequently blocked with

4 % serum. Tissue were incubated with a mouse anti-human mtTFA antibody (1:200, Cat. 119684, abcam) and a mouse anti-human MTCO2 antibody (1:200, Cat. 110258, abcam) at 4 °C overnight, followed by staining with a species-matched secondary Alexa Fluor 555-labeled donkey anti-mouse (1:400, Cat. A-31570, ThermoFisher SCIENTIFIC) and a DAPI (Cat. 10236276001, Roche). Slides were mounted with VECTASHIELD (Cat. H-1000, VECTOR). Signals were detected by fluorescence microscope equipped with a camera (Nikon, DS-QilMC). Images were analyzed by using an Adobe Photoshop software (CC 2019, Adobe) program.

Viruses

Lentiviruses encoding wild-type Flag-*EGLN3* and catalytic dead Flag-*EGLN3* with the H196A mutation (Flag-EGLN3-H196A) were generated via TOPO cloning using pLenti6.3 backbone from Invitrogen (Life Technologies).

Immunoblot analysis

The lysis of cell lines, mouse and human tissue was performed in EBC buffer (50 mM Tris at pH 8.0, 120mM NaCl, 0.5% NP-40) containing phosphatase inhibitors (Catalog: 04906837001, Sigma) and protease inhibitors (Catalog: 11697498001 Roche Life Science). Proteins were quantified by Bradford assay, and samples containing equal protein amounts were immunoblotted using previously described methodology [52]. Quantification of western blots was performed by Image J (Supplementary Information Fig.2)

Antibodies used: Rabbit monoclonal anti-TFAM (1:1000, Cell Signaling Technology, Cat# 8076), Rabbit polyclonal anti-PKA C-α (1:1000, Cell Signaling Technology, Cat# 4782), Rabbit monoclonal anti-PHD-2/Egln1 (1:500, Cell Signaling Technology, Cat# 4835), Rabbit monoclonal anti-HIF2α (1:1000, Cell Signaling Technology, Cat# 7096), Rabbit polyclonal anti-TOM20 (1:2000, Cell Signaling Technology, Cat# 13929), Rabbit polyclonal anti-TFAM (1:1000, Abcam, Cat# ab131607), Mouse monoclonal anti-GAPDH (1:2000, Abcam, Cat# ab8245), Mouse monoclonal anti-OXPHOS (1:1000, Abcam Cat# ab110413), Mouse monoclonal anti-MT-CO1 (1:1000, Abcam Cat# ab14705), Rabbit polyclonal anti-MT-CO2 (1:1000, Abcam Cat# ab91317), Rabbit polyclonal anti-MT-ND1 (1:1000, Abcam Cat# ab181848), Rabbit polyclonal anti-MT-ATP6 (1:1000, Abcam Cat# ab192423), Rabbit polyclonal anti-MT-CYB (1:1000, Abcam Cat# ab81215), Rabbit polyclonal anti-LONP1 (1:1000, Abcam Cat# ab103809), Rabbit polyclonal anti-Tyrosine Hydroxylase (1:1000, Abcam Cat# ab112), Rabbit polyclonal anti-Hydroxyproline (1:1000, Abcam, Cat# ab37067,Lot: GR3215743-1 GR3179915-1), Rabbit monoclonal anti-Cyclin D1 (1:1000, Abcam Cat# ab134175), Rabbit polyclonal anti-HIF1α (1:500, Novus Biologicals,Cat# NB100-479), Rabbit polyclonal anti-HIF2α (1:500, Novus Biologicals, Cat# NB100-122), Mouse monoclonal anti-alpha-Tubulin (1:2000, Sigma-Aldrich, Cat# T5168), Mouse monoclonal anti-HA (1:1000, Sigma-Aldrich, Cat# H9658), Rabbit polyclonal anti-Flag (1:1000, Sigma-Aldrich, Cat# F7425), Mouse monoclonal anti-PGC1α (1:1000, Millipore, Cat# ST1202), Mouse monoclonal anti-VHL (1:500, BD Biosciences, Cat# 556347), Mouse monoclonal anti-VHL (1:1000, BD Biosciences, Cat# 564183), Rabbit polyclonal anti-EGLN2 (1:500, Affinity Biosciences, Cat# DF7918), Mouse monoclonal anti-TUJ1 (1:2000, Covance, Cat# MMS-435P), Mouse monoclonal anti-c-Myc (1:1000, Thermo

Fisher Scientific, Cat# 13-2500), Mouse monoclonal anti-p-Ser (16B4) (1:500, Santa Cruz Biotechnology, Cat# sc-81514).

Proteomics analyses by nanoLC-MS/MS

Liquid chromatography tandem mass spectrometry (nanoLC-MS/MS) including database search for protein identification and quantification were performed out at the Proteomics Biomedicum core facility, Karolinska Institutet, Stockholm. For protein extraction human tissues were homogenized and lysed in EBC buffer (50 mM Tris, pH 8; 0.5% NP-40 and 120 mM NaCl) and proteins in supernatant were precipitated with chilled acetone at -20 °C overnight. Proteins (50 µg) were solubilized in 1 M urea (Sigma-Aldrich), 50 mM ammonium bicarbonate in 10% acetonitrile (AcN) and reduced with dithiothreitol (DTT) to a final concentration of 5 mM by incubation for 1 hour at 25°C and alkylated with iodoacetamide to a final concentration of 15 mM via incubation for 1 hour at 25 °C in the dark. The excess of iodoacetamide was quenched by adding an 10 mM DTT.

Digestion was performed with 1.5 µg trypsin (final enzyme to protein ratio 1:30) at 37 °C overnight followed by additional proteolysis with 1 µg Lys-C at 37 °C for 6 hours. After acidification with formic acid (5% final concentration) the tryptic peptides were cleaned with C18 HyperSep Filter Plate, bed volume 40 µL (Thermo Scientific) and dried in a speedvac (miVac, Thermo Scientific).

TMT-10plex reagents (Thermo Scientific) in 100 µg aliquots were dissolved in 30 µL dry AcN, scrambled and mixed with 25 µg digested samples dissolved in 70 µL of 50 mM TEAB (resulting final 30% AcN), followed by incubation at 22°C for 2 hours at 450 rpm. The reaction was then quenched with 11 µL of 5% hydroxylamine at 22 °C for 15 min at 450 rpm. The labeled samples were pooled and dried in a speedvac (miVac, Thermo Scientific).

The TMT-labeled tryptic peptides were dissolved in 2% AcN/0.1% formic acid at 1 µg/µL and 2 µL samples were injected in an Ultimate 3000 nano-flow LC system online coupled to an Orbitrap Fusion mass spectrometer (Thermo Scientific). Peptides were chromatographic separated by a 50 cm long C18 EASY spray column (Thermo Scientific), and 4-26% AcN for 120 min, 26-95% AcN for 5 min, and 95% AcN for 8 min at a flow rate of 300 nL/min. The mass spectrum ranged from m/z 375 to 1600, acquired with a resolution of R=120,000 (at m/z 200), followed by data-dependent HCD fragmentations of precursor ions with a charge state 2+ to 7+, using 45 s dynamic exclusion. The tandem mass scans were acquired with a resolution of R=50,000, targeting 5x104 ions, setting isolation width to m/z 1.4 and normalized collision energy to 35%. Protein identification and quantification was perfomed with Proteome Discoverer v2.3 with human SwissProt protein databases (21,008 entries) using the Mascot 2.5.1 search engine (Matrix Science Ltd.). Parameters: up to two missed cleavage sites for trypsin, precursor mass tolerance 10 ppm, and 0.02 Da for the HCD fragment ions. For quantification both unique and razor peptides were requested.

Protein identification and quantification

Protein identification and quantification was perfomed with Proteome Discoverer v2.3 with human SwissProt protein databases (21,008 entries) using the Mascot 2.5.1 search engine

(Matrix Science Ltd.). Parameters: up to two missed cleavage sites for trypsin, precursor mass tolerance 10 ppm, 0.02 Da for the HCD fragment ions. Quantifications used both unique and razor peptides. Mass spectrometric analysis and database search for protein identification and quantification were performed by Proteomics Biomedicum core facility, Karolinska Institutet, Stockholm.

Pathway analysis

According to the fold change of the protein abundance in human *VHL* mutant PPGL compared to *VHL* wild-type PPGL, top 50 significantly regulated proteins (p value < 0.05, two-tailed unpaired *t* test) were selected for protein network analysis. STRING v10.5 was used to map top 50 significantly regulated proteins in human PCC/PGL tumors onto protein-protein interaction networks (http://string-db.org) with medium confidence threshold (0.4). To identify enriched gene ontology terms and KEGG pathways, in-built gene set enrichment analysis with the whole genome background was used.

Go-term enrichment in cellular component of significantly down regulated proteins (p value < 0.0001, two-tailed unpaired *t* test) in *VHL*-null and *VHL-L188V* 786-O cells were performed using DAVID and plotted using REVIGO. GO-term enrichment was performed using DAVID with the full human proteome supplied by DAVID used as the background list, and plotted to reduce redundancy using ReviGo. The size of the bubbles is indicative of the number of proteins annotated with that GO term; bubbles are color coded according to significance.

In vitro hydroxylation of full length TFAM and ^{35}S-VHL capture

In vitro hydroxylation and S^{35} capture have been recently described **[20].** In short, Myc-TFAM, ^{35}S-HA-VHL, Flag-EGLN3 WT, Flag-EGLN3 catalytic dead mutant were synthesized by *in vitro* transcription /translation (IVT) reactions using TnT® T7 Quick Master Mix and used as substrates. IVT was added to 300μL hydroxylation reaction buffer and 100 μM FeCl2, 2 mM Ascorbate and 5 mM 2-oxolgutarate. 15 μL IVT EGLN3 were added to the hydroxylation reaction for 2 hours at room temperature. 500 μL EBC lysis buffer stopped to the hydroxylation reaction and 15 μL IVT-synthesized ^{35}S-HA-VHL was added subsequently and incubated for 2 hours. Myc-TFAM was immunoprecipitated with anti-c-Myc antibody overnight at 4 °C with rotation and captured with 70 μL (50% slurry) protein G beads. Beads pellet was washed five times with immunoprecipitation buffer (0.5% NP-40, 150 mM NaCl, 10 mM Tris-HCl). Immunoprecipitated protein complexes were eluted with Laemmli buffer, boiled and centrifuged. Supernatant was analysed by immunoblot or ^{35}S autoradiography shown in Figure 4a.

Peptide synthesis

The following biotinylated peptides were synthesized by peptides&elephants GmbH:

Naïve TFAM: -SPFSFVYLPRWFSSVLASCPKKPVSSYLRFSKEQLPIFKA

TFAM P50A-Mutant: -SPFSFVYLPRWFSSVLASCAKKPVSSYLRFSKEQLPIFKA

TFAM P53A-Mutant: -SPFSFVYLPRWFSSVLASCPKKAVSSYLRFSKEQLPIFKA

TFAM P66A-Mutant: -SPFSFVYLPRWFSSVLASCPKKPVSSYLRFSKEQLAIFKA

TFAM P53/66A-double Mutant:

-SPFSFVYLPRWFSSVLASCPKKAVSSYLRFSKEQLAIFKA

Hydroxy-TFAM-P-OH-53/66:

-SPFSFVYLPRWFSSVLASCPKKP(OH)VSSYLRFSKEQLP(OH)IFKA

Naïve HIF1α: DLDLEMLAPYIPMDDDFQLR

Hydroxy- HIF1α-P-OH 564: DLDLEMLAP(OH)YIPMDDDFQLR

Naïve HIF2α: FNELDLETLAPYIPMDGEDFQLS

Hydroxy- HIF2α-P-OH 531: FNELDLETLAP(OH)YIPMDGEDFQLS

TFAM peptide hydroxylation and ^{35}S-VHL capture

Peptide hydroxylation and ^{35}S-VHL capture shown in Fig 4d were performed as described above [**20**]**.** In short, HA-EGLN1, HA-EGLN2, HA-EGLN3 AND HA-EGLN3 catalytic dead mutant H196A were synthesized by IVT using TnT® T7 Quick Master Mix. Naïve biotin-TFAM peptide (1 μg) was conjugated with Streptavidin agarose beads (GE Healthcare Life Sciences) in 1 ml PBS at room temperature. The beads pellet was washed twice with PBS and once with hydroxylation buffer (40 mM HEPES, ph 7.4, 80 mM KCl) and resuspended with 300 μL hydroxylation reaction buffer. 15 μL IVT-synthesized HA-EGLN were added to the hydroxylation reaction as and rotated for 2 hours. 500 μL EBC buffer and 15 μL IVT-synthesized S^{35} radioactive labeled HA-VHL was added and incubated overnight at 4 °C. Samples were centrifuged and washed five times with immunoprecipitation wash buffer. Bound peptide/protein complexes were eluted with 30 μL Laemmli buffer, boiled and centrifuged. Bound ^{35}S-HA-VHL was eluted by boiling in SDS-containing sample buffer, resolved by PAGE, and detected by autoradiography.

Mass spectrometry analysis for peptide hydroxylation

The hydroxylation assay with TFAM peptide and EGLN3 shown in Figures 4c-f was performed as described above and processed as recently described [53]. In short, after hydroxylation assay, TFAM peptide conjugated beads were washed one time with hydroxylation buffer and three times with IP buffer without detergent. Peptides were digested with trypsin and directly analyzed by Mass Spectrometry on a Q-Exactive mass spectrometer connected to an Ultimate Ultra3000 chromatography system as recently described [20].

S^{35}VHL mutant capture with hydroxylated hydroxy-TFAM-P-OH-53/66

The following biotinylated peptides were used for ^{35}S-VHL mutant capture shown in Fig 4h,i and Fig S4h:

hydroxy-TFAM-P-OH-53/66, hydroxy-HIF1α-P-OH 564, hydroxy- HIF2α-P-OH 531:

Peptides were rotated for 1hour at room temperature and samples were subsequently washed twice with PBS. ^{35}S-VHL produced by IVT was captured as previously described [20] and above.

HA-VHL pulldown using hydroxylated peptides in ccRCC

HA-VHL pull down in ccRCC cells shown in Figure 4j and Figure S3i were performed with the following biotinylated peptides: naïve TFAM and naïve HIF2α as control, hydroxy-TFAM-P-OH-53/66 and hydroxy-HIF2α-P-OH. First, peptides were conjugated with streptavidin beads and incubated respectively with cell lysate for 4 hours at 4 °C with rotation. Samples were then washed 4 times with immunoprecipitation washing buffer (0.5% NP-40, 150 mM NaCl, 10 mM Tris-HCl) and eluted with 30 μL Laemmli buffer, boiled for 5 minutes and centrifuged at 8000xg for 30 seconds. The resulting supernatant was subjected to immunoblot analysis.

TFAM degradation assay by LONP1

60 μL Dynabeads His-Tag Isolation & Pulldown (#10103D) were incubated with purified His-TFAM (2 μM) for 1 hour 30 mins at room temperature with rotation. Meanwhile, Flag-EGLN3 WT, Flag-EGLN3-H196A catalytic dead mutant were synthesized by IVT as described above. His-TFAM conjugated beads were resuspended with 1 ml hydroxylation reaction buffer supplemented with 100 μM FeCl2, 2 mM Ascorbate and 5 mM 2-oxolgutarate. 75 μL unprogrammed reticulocyte lysate, IVT-synthesized wild-type EGLN3 or EGLN3-H196A mutant were added to start the hydroxylation reaction. The hydroxylation reaction was processed for 2 hours at room temperature with rotation. 1 μg HA-VHL was incubated with the reaction samples for 2 hours at room temperature with rotation and the bound proteins complexes were washed twice with distilled water and resuspended with 25 μL LONP1 degradation buffer containing 30 mM NaCl, 10 mM Hepes-KOH pH 8.0, 2 mM $MgCl_2$, 0.1 mg/ml BSA, 4 mM ATP, and 100 nM LONP1. The TFAM degradation assay by LONP1 was processed for 2 hours at 37 °C. Bound protein complexes were eluted with 30 μL of Laemmli buffer, boiled for 5 min, and centrifuged at 8,000 × g for 30 s. Eluted supernatant was analyzed by immunoblotting.

Expression Plasmids, shRNA, siRNA’s and gRNA

pcDNA3 Flag-*EGLN3*, Flag-*H196A*-mutant and pcDNA3-*VHL* including *VHL*-missense mutations have been described previously [54]. Lentivirus encoding FLAG-*EGLN3* and FLAG-*EGLN3-H196A* were generated in 293FT cells (Thermo Fisher R70007) as previously described [48]. siRNAs targeting *EglN1*, *EglN2* or *EGLN3* were generated with the following sequences: si*EGLN1*: (5'->3'): (AGCUCCUUCUACUGCUGCA)(UU); si*EGLN2*: (5'->3'): (GCCACUCUUUGACC-GGUUGCU)(UU); si*EGLN3*: (5'->3'): (CAGGUUAUGUUCGCCAC-GU)(UU). Lentivirus encoding shRNAs targeting human *EglN1*, *EglN2* and *EGLN3* were generated using the pLKO.1 plasmid using the following sequences:

EglN1 (5′-CCGGGACGACCTGATACGCCACTGTCTCGAGACAGGGCGTATCAGG-TCGTCTTTTT-3′);

EglN2 (5′-CCGGCTGGGACGTTAAGGTGCATGGCTCGAGCCATGCACCTTAACG-TCCCAGTTTTT-3)′;

EGLN3 (5′-CCGGGTTCTTCTGGTCAGATCGTAGCTCGAGCTACGATCTGACCAGA-AGAACTTTTTG-3).

sgRNA (Sigma Aldrich) sequences targeting *EPAS1* or CONTROL were cloned into pLentiCRISPR-V2 (Addgene #52961, Johan Homberg Lab provided).

sgEPAS1-EX2-T1-SS: 5'-caccgGTGCCGGCGGAGCAAGGAGA-3',

sgEPAS1-EX2-T1-AS: 5'-aaacTCTCCTTGCTCCGCCGGCACc-3';

sgEPAS1-EX2-T2-SS: 5'-caccgGATTGCCAGTCGCATGATGG-3',

sgEPAS1-EX2-T2-AS: 5'-aaacCCATCATGCGACTGGCAATCc-3',

sgCONTROL-SS: 5'-caccgCTTGTTGCGTATACGAGACT-3',

sgCONTROL-AS: 5'-aaacAGTCTCGTATACGCAACAAGc-3'.

Generation of piggybac vetor expressing wildtype and mutant *TFAM*

TFAM wildtype and P53/66A mutant ORF CDS were PCR from pReciver-M07(GeneCopoeia,EX-F0074-M09). Primers are iTFAM-F:

5'-GAATGGTCTCTCTAGCGCCGCCACCATGGCGTTTCTCCGAAGC-3'; iTFAM-R: 5'-GAATGGTCTCTCGCGTTCACAGATCCTCTTCAGAGATGAGT-3' (Integrated DNA Technologies). The PCR products and pB-TRE-empty or pB-TRE-Luc2-empty vectors (gifts from Johan Holmberg lab) were digested by NheI and MluI(New England Biolabs), after purification, the PCR products were ligated into the pB-TRE-empty or pB-TRE-Luc2-empty vector. Sequences were confirmed by Sanger method (Integrated DNA Technologies).

Generation of stable and inducible *TFAM* expression in HEK293 cells

Transposon vectors pB-TRE-*TFAM*-wt-Luc2, pB-TRE-*TFAM*-mut-Luc2 and transposase vector pCAGhypbase were transfected at the ratio of 4:1 into HEK293 cells by Lipofectamine 2000 (Invitrogen) according to the manufactory instructions. Two days later, cells were selected under 200ug/ml Hygromycin B until the blank cells were 100% dead. Then 0,9x10^5 cells were seeded into 6WD, 100ng/ml Doxycycline (Clotech) were added into the cells for 48 hours before the cells were harvested for western blot.

Co-immunoprecipitation

One confluent p150 plate of 786-O cells stably expressing *VHL* (pPC3, WT-*VHL*, *L188V-VHL*) or 786-O WT-*VHL* cells infected with lentivirus targeting *EglN1*, *EglN2 EGLN3* respectively was washed once in ice-cold PBS, trypsinized and subsequently harvested with 10 ml ice-cold PBS, collected by centrifugation (5 min at 1200 × g, 4 °C), resuspended and homogenized in EBC buffer (50 mM Tris at pH 8.0, 120 mM NaCl, 0.5% NP-40) containing protease inhibitor and phosphatase inhibitor. The lysates were centrifuged at 14,000 × g for 10 min to pellet unlysed cellular debris and the resulting supernatant was respectively incubated with HA antibody overnight at 4 °C. Samples were incubated for 5 hours with rotation at 4 °C with 70 μL (50% slurry) Protein G agarose beads (sc-2002, SANTA CRUZ) pre-washed twice with immunoprecipitation washing buffer (0.5% NP-40, 150 mM NaCl, 10 mM Tris-HCl). Samples were centrifuged at 8000 x g for 30 sec and washed five times with immunoprecipitation washing buffer (0.5% NP-40, 150 mM NaCl, 10 mM Tris-HCl). Immunoprecipitated proteins were eluted with 50 μL Laemmli buffer, boiled for 5 min and centrifuged at 8000 x g for 1 min. The resulting eluted supernatant was subjected to immunoblot analysis.

Co-immunoprecipitation using anti-hydroxyproline antibody

293FT cells were transiently transfected with plasmids encoding Flag-*TFAM* and Flag-*EGLN3* WT or catalytic-dead mutant (Mut) with or without DMOG treatment or transiently transfected with plasmids encoding Flag-TFAM and HA-*EglN1*, HA-*EglN2* and HA-*EGLN3*. Immunoprecipitation using anti-hydroxyproline antibody (HydroxyP) (Cat# ab37067; Lot: GR3215743-1, GR3179915-1) from 293FT cells shown in Fig 4b and Extended Data Fig.4a was performed as described above.

Protein kinase A (PKA) activity assay

Hydroxylated TFAM (1 μg) biotinylated peptide was conjugated with 30 μL Streptavidin agarose beads (GE Healthcare Life Sciences) in 1 ml PBS at room temperature with rotation for 1 hour. The beads pellet was washed three times with PBS and resuspended in 500 μL PBS supplemented with 1 μg purified GST-pVHL protein for 2 hours at room temperature. Subsequently, TFAM phosphorylation by PKA was assayed using PKA Kinase Activity Assay Kit (ab139435, Abcam) according to manufacturer's instructions. Samples were centrifuged at 8000 x g for 30 sec and washed three times with PBS and re-suspended with 50 μL kinase assay dilution buffer supplemented with 1 μg/μL ATP and 50 ng purified active PKA. The phosphorylation assay was processed for 40 min at room temperature with rotation and for 40 min at 30 °C. Samples were centrifuged at 8000 x g for 30 sec and washed three times with PBS and eluted with 30 μL Laemmli buffer, boiled for 5 min and centrifuged at 8000 x g for 30 sec. Eluted supernatant was analyzed by immunoblotting using pan-phospho-serine antibody (Santa Cruz: sc-81514).

Crystal violet staining for apoptosis

ccRCC 786-O and MEFs cells were treated with 3-Bromopyruvic acid or gossypol with the indicated times. Cells were washed once with PBS and then fixed and stained by crystal violet solution (0.1% crystal violet, 20% methanol, 80% dH_2O) for 45 min at room temperature and washed 4 times with PBS.

TFAM Half-life

786-O and MEFs cells were cultured in 6-well plates in 2 ml DMEM medium to reach 50% confluency. Cells were treated with 10 μM cyclohexamide at the indicated times, subsequently harvested and lysed in EBC lysis buffer. Cell lysates were then subjected to Western blot analysis with the rabbit anti-TFAM antibody.

Evaluation of mitochondrial respiration rate and extracellular acidification rate

The oxygen consumption rate (OCR) and extracellular acidification rate (ECAR) were respectively determined using Mito Stress Test Kit (Agilent, Catalog: 103015–100), Glycolysis Stress Test Kit (Agilent, Catalog: 103020-100) and an XFe96 Extracellular Flux Analyzer (Seahorse Bioscience, Billerica, MA, USA). Then the XFe96 Sensor Cartridge (Catalog: 102416-100) was hydrated using 200 µL of sterile calibrant (Catalog: 100840-000) in each well of the utility plate. Assembled sensor cartridge and utility plate were kept in a 37 °C CO_2-free incubator overnight. 786-O and MEFs cells were seeded into XFe96 cell culture microplates (Catalog: 101085-004) at the density of 10,000 cells/well and allowed to adhere to plate overnight. The cell culture medium was replaced with Seahorse XF DMEM medium (Catalog: 103575-100) containing 10 mM glucose, 2 mM glutamine, 1 mM pyruvate and placed in a 37 °C CO_2-free incubator for 1 hour. Finally, after preincubation, oxygen consumption rate (OCR) was measured in the Agilent’s Seahorse Bioscience XF96 Extracellular Flux Analyzer (Agilent Technologies) from the baseline OCR determination and subsequent sequential injections of three compounds that affect the cellular bioenergetic processes, as follows: 20 µL of oligomycin (10 µM) in port A, 22 µL of FCCP (10 µM) in port B and 25 µL of Rotenone/AntimycinA (5 µM) in port C, according to the manufacturer’s instructions and protocols. Extracellular acidification rate (ECAR) was measured from the baseline ECAR determination and subsequent sequential injections of three compounds as follows: 20 µL of glucose (100 mM) in port A, 22 µL of oligomycin (10 µM) in port B and 25 µL of 2-deoxy-glucose (2-DG) (500 µM) in port C, according to the manufacturer’s instructions and protocols.

Proximity Ligation Assay (PLA), Image Acquisition and Image Processing

786-0 cells (pRC3 and *VHL* WT) were plated on glass coverslips. Cells were incubated with 100nM MitoTracker Red CMXRos (Invitrogen, Waltham, MA) for 1h at 37°C and fixed with 4% paraformaldehyde and permeabilized using 0.1% Triton X-100 (Sigma-Aldrich, St. Louis, MO) in PBS. After incubation with TFAM and VHL antibodies (1:500 #8076, Cell Signalling Technology, CO; and 1:1000 #564183, Beckton Dickinson, Franklin Lakes, NJ, respectively) at +4°C overnight, the PLA assay was performed using Duolink® In Situ PLA® Probe Anti-Rabbit PLUS and Anti-Mouse MINUS, and Duolink® In Situ Detection Reagents Green (Sigma-Aldrich, St. Louis, MO) following the manufacturer’s instructions. The immunofluorescence signals were acquired by LSM 700 Laser Scanning Confocal System with Zeiss Observer Z1 Inverted Phase Contrast Fluorescence Microscope (ZEISS, Oberkochen, Germany) using 63x magnification. Twenty images of randomly selected areas per cell line were taken. Each fluorophore channel was pseudo-colored in ZEN2 (ZEISS, Oberkochen, Germany), exported as JPEG, and analyzed using the CellProfiler 4.2.0 cell image analysis software (Broad Institute of Harvard and MIT, Boston, MA). The number of PLA signals per cell was quantified from the maximal intensity projection of each image. Statistical analysis was performed using GraphPad Prism 9 software to calculate the nonparametric Mann–Whitney U test (GraphPad Software, San Diego, CA). The P value <0.05 was considered significant.

Mitochondrial fractionation

The mitochondria were isolated as previously described [55]. The cells were collected and resuspended in the MSE buffer (109mg/ml mannitol (Cat NO. M4125, Sigma), 10mM Tris pH7.4, 1mM EDTA) containing 0.1% BSA (Cat NO. A7030, Sigma). The cells were homogenized followed by low speed centrifugation to remove the cell debris. Mitochondria were pelleted and washed with MSE buffer. One-third of the mitochondrial fraction was pelleted as ‘untreated mitochondrial fraction’. Two-thirds of the mitochondria were digested with 15ug/ml Proteinase K (Cat NO. 25530049, ThermoFisher). Half of them were treated with 1mM PMSF followed by wash twice with MSE buffer containing PMSF and another half was treated with 1% Triton-X100. The total cell and mitochondrial were lysed in the lysis buffer (Cat NO. FLAGIPT1, Sigma) containing protease inhibitor cocktail (Roche) prior to loading on the SDS-PAGE.

Chemical reagents

Gossypol (G8761-100 mg), H-89 dihydrochloride hydrate (B1427), Bromopyruvic acid (3-BP) and Cycloheximide (C4859) were purchased from Sigma-Aldrich. Bortezomib (B-1408) was purchased from LC Laboratories. MitoTracker™ Red CMXRos (Cat. M7512) and MitoTracker™ Green FM (Cat. M7514) were purchased from Thermo Fisher Scientific. Forskolin (#3828) was purchased from Cell Signaling Technology.

Ethical Considerations

Collection and analyses of human samples (normal adrenal tissues, PCCs and PGLs) are covered by the ethical approvals Dnr 01-136, KI forskningsetikkommitté Nord and Dnr 2020-04226. All samples were obtained following an informed patient consent. Ethical permits for animal studies were approved by the appropriate local and national authorities – Jordbruksverket, Sweden.

Quantification and Statistical Analysis—The hypothesis that the percentage of mitochondrial proteins was significantly lower in both *VHL*-null and *VHL188V* cells compared to *VHL* wild-type expressing cells was tested. We tested the null hypothesis that there is no difference between the proportion of mitochondrial proteins with significantly higher and significantly lower abundances between the study cases and control (e.g. wild type), using two-tailed Fisher's exact tests. The null hypothesis was rejected using a p-value threshold of 0.01. Further, we tested the hypothesis that 1) the proportion of HIF-independent (e.g. L188V) and not-HIF-independent (e.g. *VHL*-null excluding intersecting *VHL-L188V*) significantly downregulated mitochondrial proteins, and 2) the proportion of HIF-independent (e.g. *VHL* mutated PPGL intersecting *VHL-L188V*) and not-HIF-independent (e.g. *VHL* mutated PPGL excluding intersecting *VHL-L188V*) significantly downregulated mitochondrial proteins, are not different than the same proportions in significantly downregulated non-mitochondrial proteins. These two-tailed Fisher's exact tests and were rejected using a p-value threshold of 0.01. Fisher's tests were conducted using the Scipy package version 1.0.0, in python 2.7.

Analysis of the quantitative proteomics data was performed as previously described. Briefly, Tandem Mass Tag (TMT) reporter was used for mass spectrometry-based peptide quantification. TMT reporter abundance values were normalized to the total abundance of the same TMT channel. Quality check was performed by calculating the variation (CV) between the replicates as well as by building PCA models to verify the small data spread between the replicates. The median values of the replicates in each condition were used for fold change calculations. The significance of protein abundance difference between two different conditions was calculated by two-tailed unpaired *t* test. Mitochondrial proteins were selected according to the cellular component gene ontology term searched by Proteome Discoverer v2.3 in the human SwissProt protein database.

Extended Data

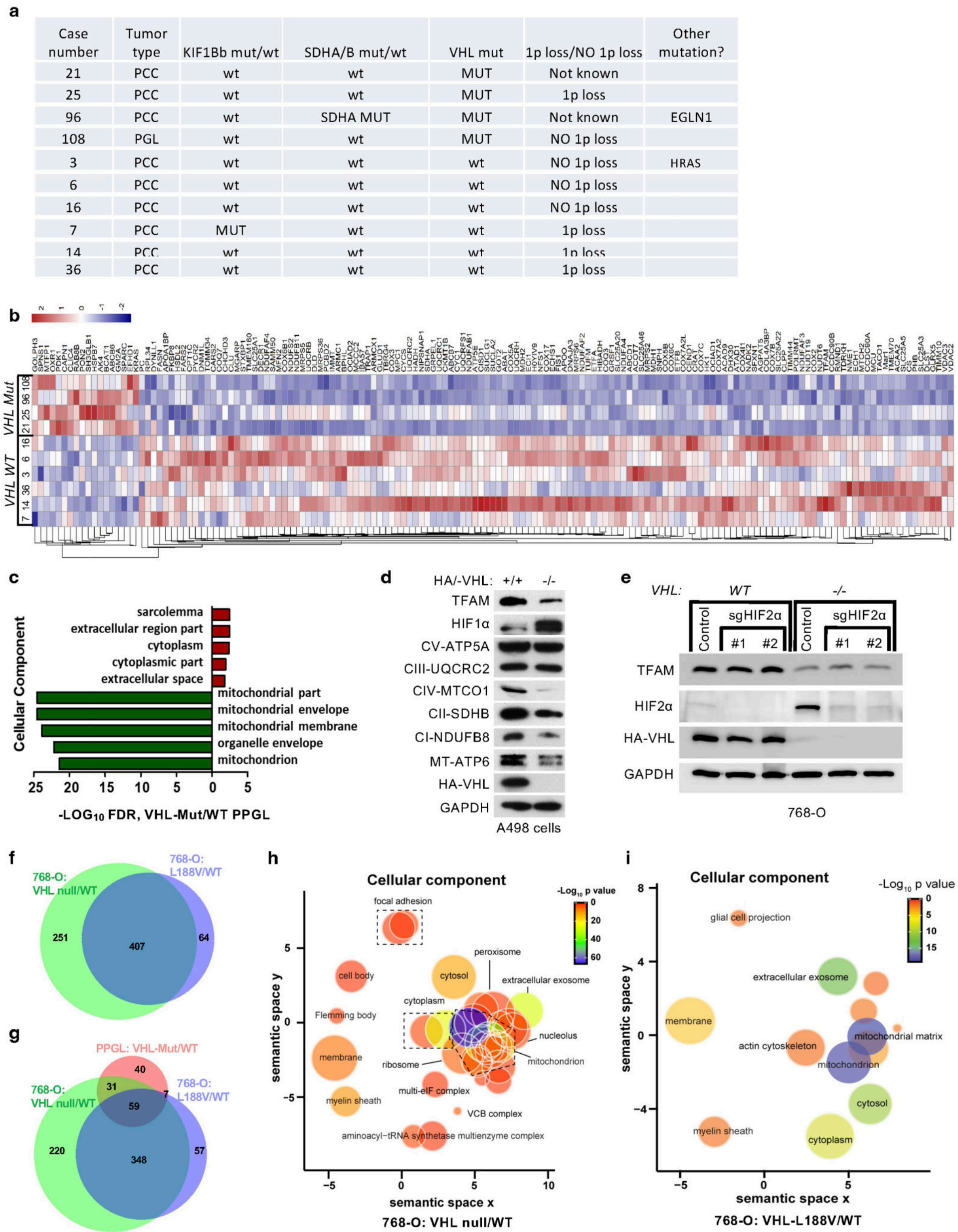

Case number	Tumor type	KIF1Bb mut/wt	SDHA/B mut/wt	VHL mut	1p loss/NO 1p loss	Other mutation?
21	PCC	wt	wt	MUT	Not known	
25	PCC	wt	wt	MUT	1p loss	
96	PCC	wt	SDHA MUT	MUT	Not known	EGLN1
108	PGL	wt	wt	MUT	NO 1p loss	
3	PCC	wt	wt	wt	NO 1p loss	HRAS
6	PCC	wt	wt	wt	NO 1p loss	
16	PCC	wt	wt	wt	NO 1p loss	
7	PCC	MUT	wt	wt	1p loss	
14	PCC	wt	wt	wt	1p loss	
36	PCC	wt	wt	wt	1p loss	

Extended Data Fig. 1. VHL regulates of mitochondrial mass independent of HIFa.

(a) List human primary PPGL tumors with characterized mutation status and 1p36 status that were analyzed by bynanoLC-MS/MS in Figure 1A-D. wt = wild-type. (b) Heatmap of significantly regulated mitochondrial proteins in VHL-mutant compared to VHL wild-type PPGL tumors ($p < 0.05$, two-tailed unpaired t test). (c) Top 5 cellular component of top 50 up (red)- and down (green)-regulated proteins for human VHL mutant PCC/PGL tumors compared to VHL wild type PCC/PGL tumors according to the false discovery rate (FDR). Medium confidence threshold (0.4) was used to define protein-protein interactions. (d) Immunoblot analysis of A498 VHL-null cells (−/−) stably transfected to generate HA-VHL (WT). n = 3 biological independent experiments. (e) Immunoblot analysis of 786-O cells with indicated genotype stably transduced with lentivirus encoding sgRNA targeting HIF2α. n = 3 biological independent experiments. (f) Venn diagram representing significantly downregulated proteins shared in VHL-null 786-O cells with type 2C VHL-L188V mutant cells and (g) shared with VHL mutant PPGL. (h, i) GO term enrichment in cellular component of 393 significantly down-regulated proteins (p values < 0.0001, two-tailed unpaired t test) comparing VHL-null to VHL-WT cells (h) and 200 significantly down-regulated proteins (p values < 0.0001,two-tailed unpaired t test) comparing VHL-L188V to VHL-WT cells (i) performed using DAVID and plotted using REVIGO. The size of the bubbles is indicative of the number of proteins annotated with that GO term; bubbles are color coded according to significance.

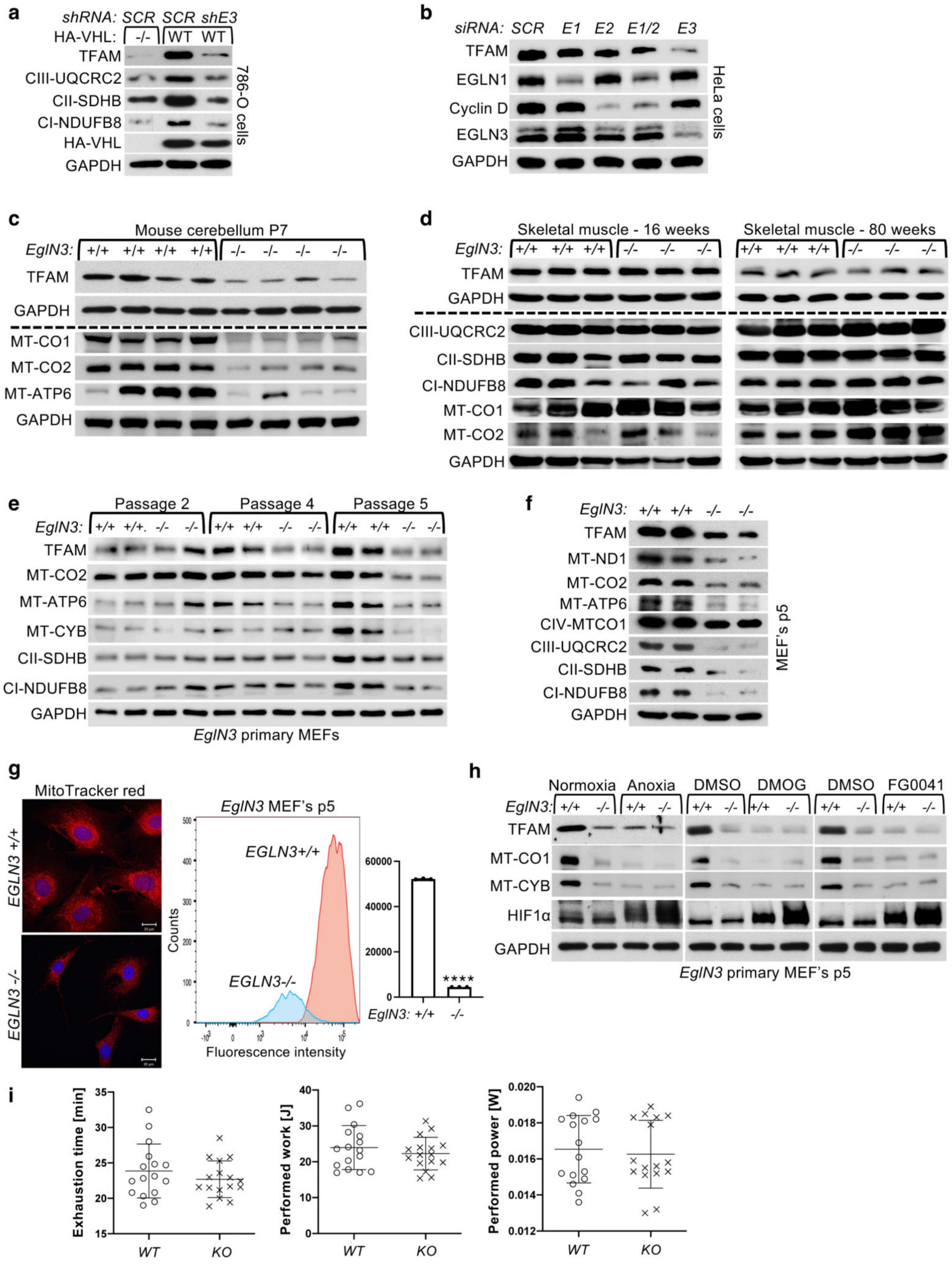

Extended Data Fig. 2. VHL regulation of mitochondrial mass is hydroxylation and EglN3 dependent.

(a) Immunoblot analysis of 786-O cells with indicated VHL status transduced with lentiviral pL.KO shRNA targeting EGLN3 (shE3) or no targeting control (SCR). n = 3 biological independent experiments. (b) Immunoblot analysis of HeLa cells transduced with lentiviral pL.KO shRNA targeting EGLN1, EGLN2, EGLN3 or no targeting control. n = 3 biological independent experiments. (c) Immunoblot analysis of mouse cerebellum of indicated genotype. n = 4 biologically independent EGLN3 wildtype or knockout mice. (d) Immunoblot analysis of mouse skeletal muscles of indicated genotype. n = 3 biologically independent EGLN3 wildtype or knockout mice. (e) Immunoblot of primary EglN3-MEFs of indicated genotype with different passages. n = 3 biological independent experiments. (f) Immunoblot analysis of primary EGLN3-MEFs of indicated genotype. n = 3 biological independent experiments. (g) Left: Fluorescence images of primary EGLN3-MEFs of indicated genotype. Mitochondria were stained by MitoTracker Red. Right: Flow cytometry analysis of MitoTracker Green-stained primary MEFs of indicated genotype. Data are presented as mean values ± S.D. Two-tailed unpaired t test. ****p <0.0001. n = 3 biological independent experiments. (h) Immunoblot of EGLN3 primary MEFs with indicated genotype upon normoxic or anoxic conditions for 16h or treated with 1 mM DMOG or 50 μM FG0041 for 8 h. n = 3 biological independent experiments. (i) In contrast young adult, KO mice (18-19 weeks of age) show a comparable exhaustion time, performed work and performed power (n=16 per genotype, male mice). Data represent means ± SD and individual measurements.

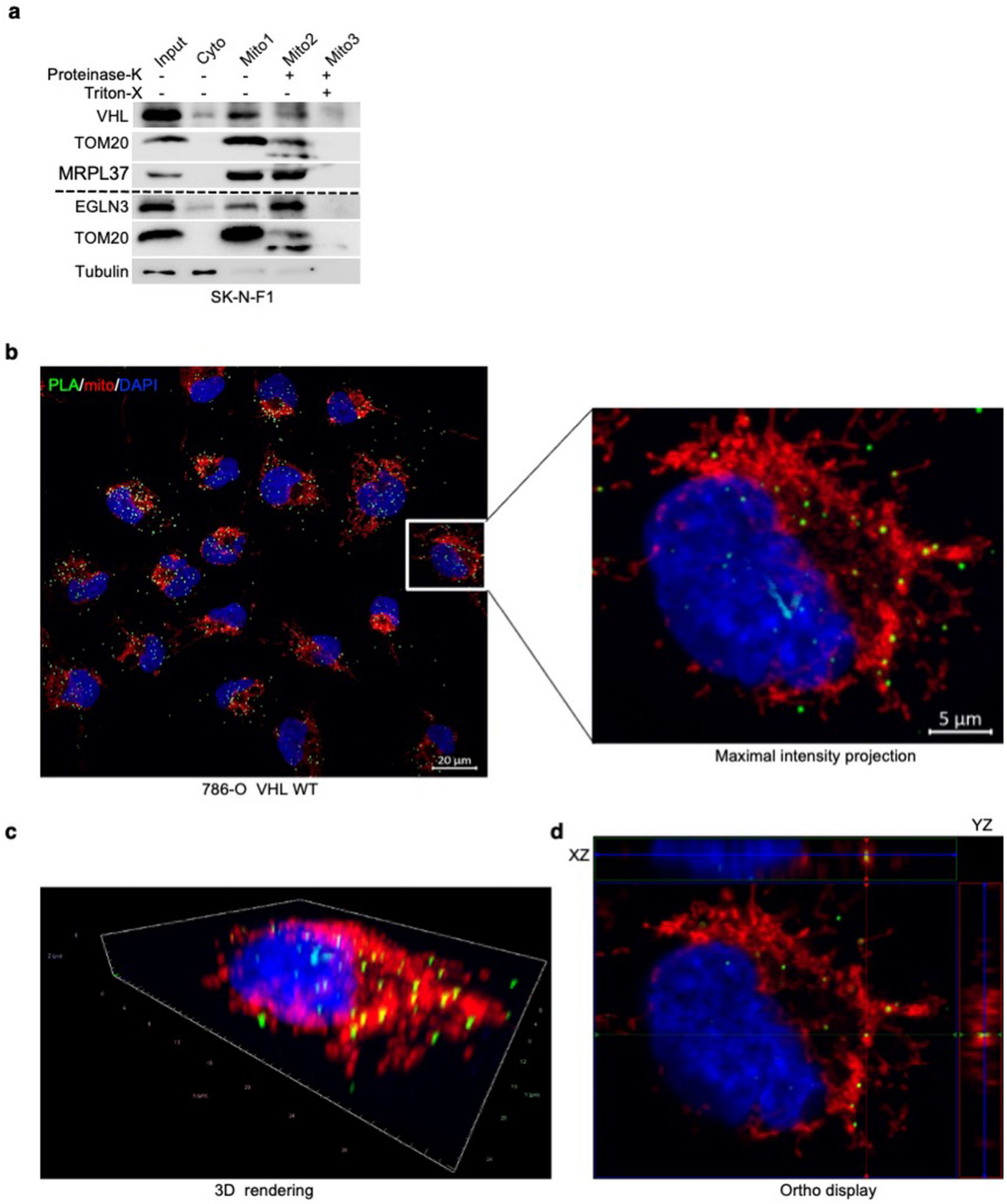

Extended Data Fig. 3. VHL interacts with TFAM within mitochondria.

(a) Immunoblot analysis of subcellular fractionation of SK-N-F1 cells. Cell lysates were fractionated into cytosolic and mitochondrial fractions. In addition, aliquots of the mitochondrial fractions were treated with 25 μg/ml Proteinase K with or without treatment with 1% Triton X-100. Fractions were analyzed by western blotting and the localization of VHL or EglN3 was assessed in comparison to that of protein markers of the cytosol (tubulin), outer mitochondrial membrane (TOM20), and mitochondrial matrix (mitochondrial ribosomal protein MRPL37). n = 3 biological independent experiments.

(b) Representative images of proximity ligation assay (PLA) signal (green), DAPI (blue) and MitoTracker Red (red) triple staining in 786-0 cells expressing VHL wildtype. The images show the maximal intensity projection of the signal/staining. (c) 3D rendering and (d) Orthogonal view showing co-localization of PLA signal in mitochondria (yellow). Magnification 63x; scale bar: 5 μm. (b-d) Similar results were seen more than three times.

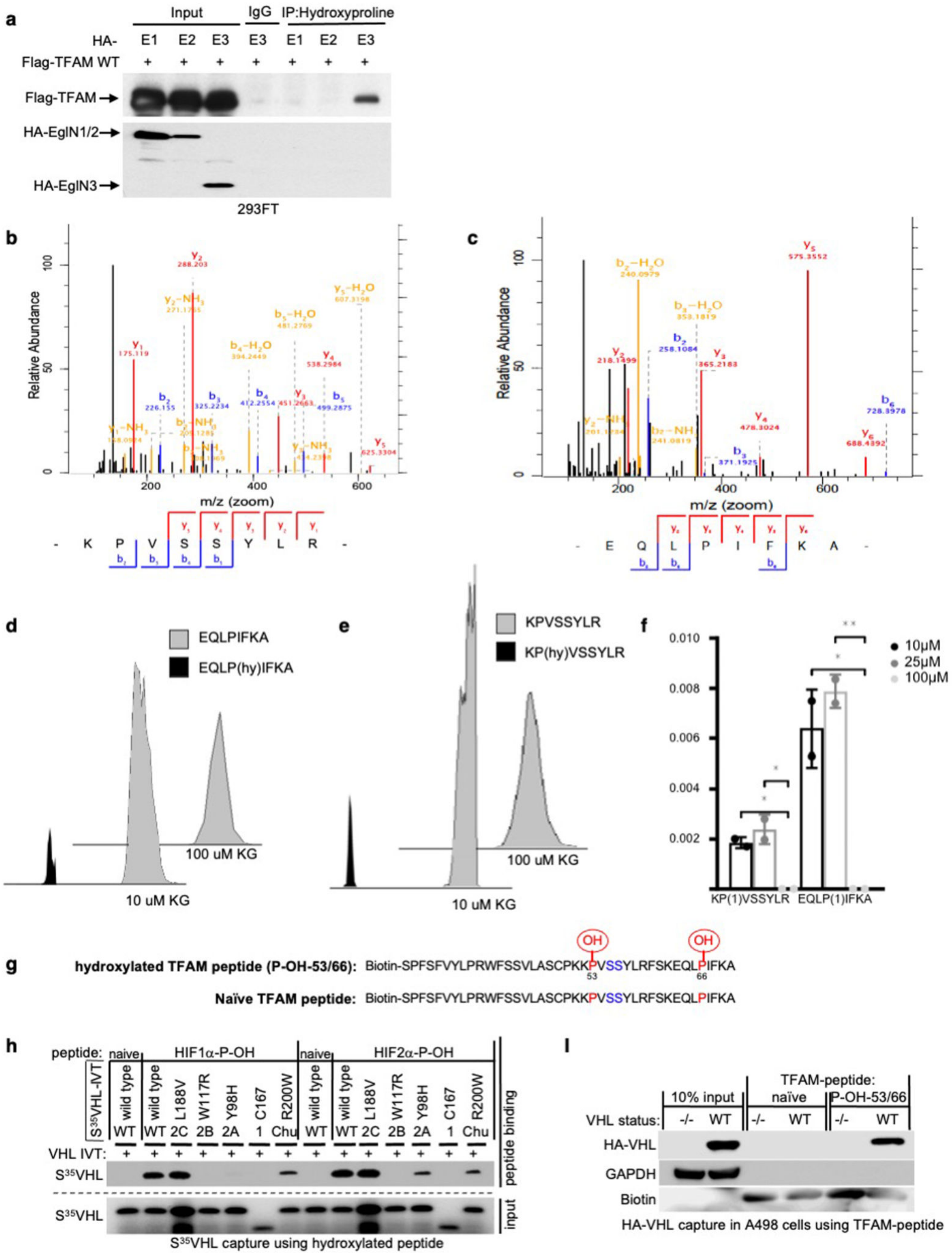

Extended Data Fig. 4. TFAM is hydroxylated by EglN3 at Proline 53/66 causing pVHL recognition.

(a) Immunoprecipitation using antihydroxyproline antibody (HydroxyP) from 293FT cells that were transiently transfected with plasmids encoding Flag-TFAM and HA-EGLN1, HA-EGLN2 and HA-EGLN3. Immunoblots show co-immunoprecipitation of Flag-TFAM. n = 3 biological independent experiments. (b-c) Mass spectrometry of unmodified biotinylated TFAM-peptide-30-70. Shown is the representative fragmentation peptide spectra of non-hydroxylated Biotin-KPVSSYLR (b) and non-hydroxylated Biotin-EQLPIFKA (c). (d,e) Extracted ion chromatogram of biotinylated unmodified and mono hydroxylated proline residues 53 (d) or proline residues 66 (e) TFAM peptide following an in vitro hydroxylation reaction with EglN3 with indicated concentration of ϒ-ketoglutarate (KG). Control indicates unmodified biotinylated TFAM-peptide that was not subjected to EGLN3 hydroxylation. (f) Hydroxylation levels of proline residues 53 and 66 of TFAM peptide following hydroxylation with EGLN3 generated via IVT with indicated concentration of KG. Data are presented as mean values ± SD. n = 3 biological experiments. One way ANOVA Tukey's Multiple Comparison Test. *p <0.05, **p <0.01. p=0.0288, p=0.0143, p=0.0148, p=0.0082. (g) Schematic illustration of synthetic biotinylated TFAM peptide hydroxylated at P-OH-53 and P-OH-66 and naïve TFAM peptide. (h) Autoradiograms showing recovery of 35S-labeled VHL protein (WT) or corresponding disease mutants (as indicated) bound to biotinylated HIF1α peptide (residues 556 to 575) with hydroxylated proline 564 (HIF1α-P-OH) and HIF2α peptide (residues 521 to 543) with hydroxylated proline 531 (HIF2α-P-OH). Biotinylated HIF1α and HIF2α naïve peptides were used as negative controls. n = 3 biological independent experiments. (i) Peptide pulldown using biotinylated TFAM-P-OH-53/66 peptide incubated with whole-cell lysates from A498 cells expressing HA-VHL WT or empty control. Biotinylated TFAM naïve peptide was used as negative control. n = 3 biological independent experiments.

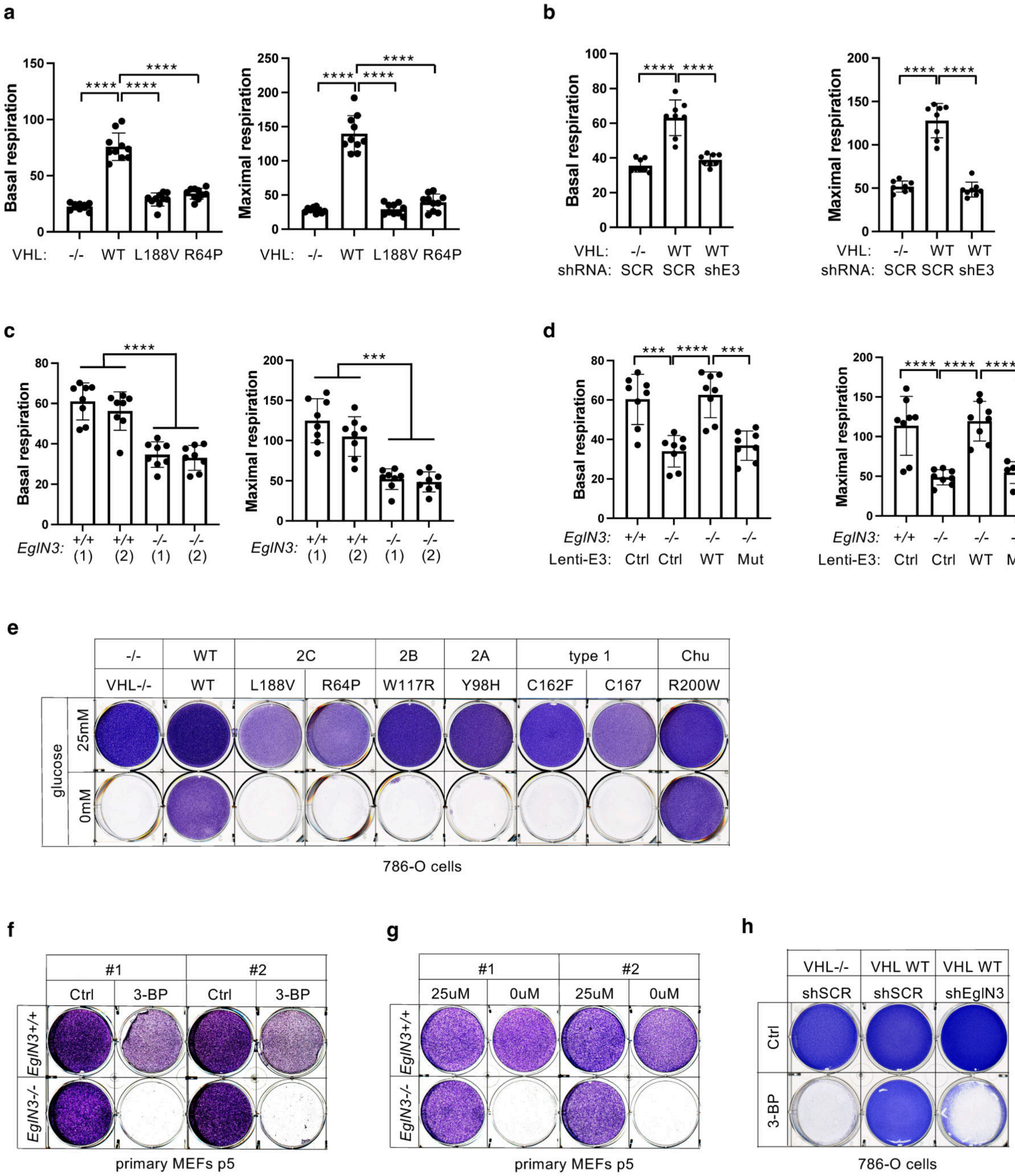

Extended Data Fig. 5. VHL restores cellular oxygen consumption rate.

(a) Seahorse XF-96 analysis of oxygen consumption rate (OCR). Mitochondrial respiration reflected by OCR levels was detected in 786-O cells with indicated genotype. The rates of basal respiration and maximal respiratory capacity were respectively quantified by normalization of amount of cells. One way ANOVA Tukey's Multiple Comparison Test. ****p <0.0001. (b) Seahorse XF-96 analysis of oxygen consumption rate (OCR) of 786-O cells with indicated VHL status transduced with lentiviral pL.KO shRNA targeting EGLN3 or no targeting control. The rates of basal respiration and maximal respiratory capacity were respectively quantified as described above. One way ANOVA Tukey's Multiple Comparison Test. ****p <0.0001. (c) Seahorse XF-96 analysis of oxygen consumption rate (OCR) of primary EGLN3+/+ and EGLN3-/- MEFs. The rates of basal respiration and maximal respiratory capacity were respectively quantified by normalization of amount of cells. One way ANOVA Tukey's Multiple Comparison Test. ***p <0.001, ****p <0.0001. (d) Seahorse XF-96 analysis of oxygen consumption rate (OCR) of primary EGLN3-MEFs of indicated genotype stably transduced with lentivirus encoding EGLN3 WT, catalytic death mutant or empty control. The rates of basal respiration and maximal respiratory capacity were respectively quantified as described above. ***p <0.001, ****p <0.0001. a-d, data are presented as mean values ± SD. n = 3 biological independent experiments. (e) Crystal violet staining of 786-O cells with indicated VHL status treated with high glucose (25 mM) or no glucose respectively for 36 hours. (f) Crystal violet staining of primary EGLN3+/+ and EGLN3-/- MEFs treated with 100 μM 3-bromopyruvic acid (3-BP) for 4 hours. (g) Crystal violet staining of primary EGLN3+/+ and EGLN3-/- MEFs treated with high glucose (25μM) or no glucose (0μM) respectively for 48 hours. (h) Crystal violet staining of 786-O cells with indicated VHL status transduced with lentiviral pL.KO shRNA targeting EGLN3 or no targeting control, treated with 100 μM 3-bromopyruvic acid (3-BP) for 4 hours.

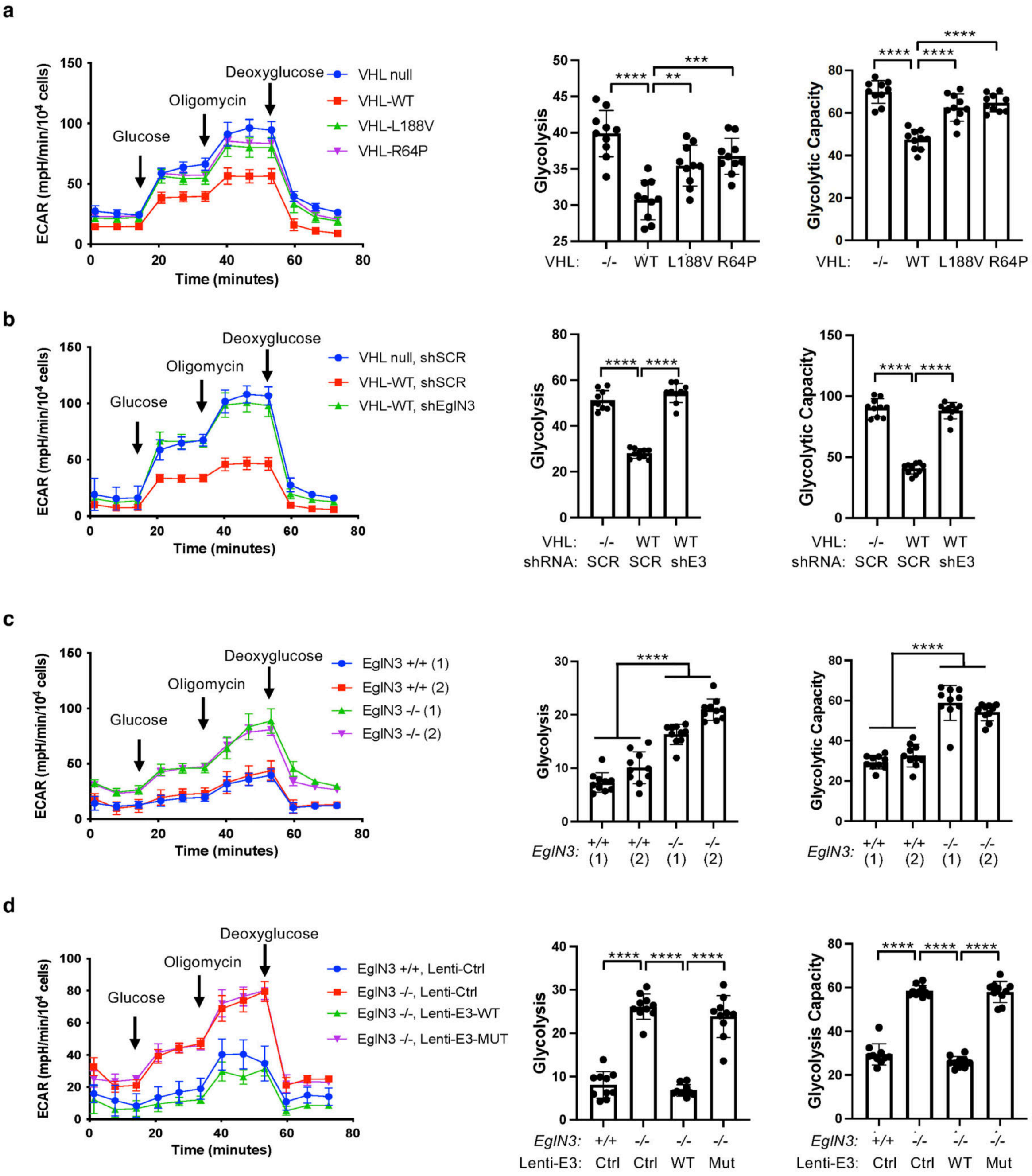

Extended Data Fig. 6. VHL decreases glycolysis.

(a) Extracellular acidification rate (ECAR) of 786-O cells with indicated genotype was monitored using the Seahorse XF-96 Extracellular Flux Analyzer with the sequential injection of glucose (10 mM), oligomycin (1 μM) and 2-deoxy-glucose (2-DG) (50 μM). The rates of glycolysis and glycolysis capacity were respectively quantified by normalization of amount of cells. One way ANOVA Tukey's Multiple Comparison Test. $^{**}p = 0.003$, $^{***}p = 0.0002$, $^{****}p < 0.0001$. (b) Extracellular acidification rate (ECAR) of 786-O cells with indicated VHL status transduced with lentiviral pL.KO shRNA targeting EGLN3 or no targeting control was measured as described above. The rates of glycolysis and glycolysis capacity were respectively quantified by normalization of amount of cells. One way ANOVA Tukey's Multiple Comparison Test. ****p <0.0001. (c) Extracellular acidification rate (ECAR) of primary EGLN3+/+ and EGLN3-/- MEFs. The rates of glycolysis and glycolysis capacity were respectively quantified by normalization of amount of cells. One way ANOVA Tukey's Multiple Comparison Test. ****p <0.0001. (d) Extracellular acidification rate (ECAR) of primary EGLN3-MEFs of indicated genotype stably transduced with lentivirus encoding EGLN3 WT, catalytic death mutant or empty control was monitored as described above. The rates of glycolysis and glycolysis capacity were respectively quantified by normalization of amount of cells. One way ANOVA Tukey's Multiple Comparison Test. ****p <0.0001. a-d, data are presented as mean values ± SD. n = 3 biological independent experiments.

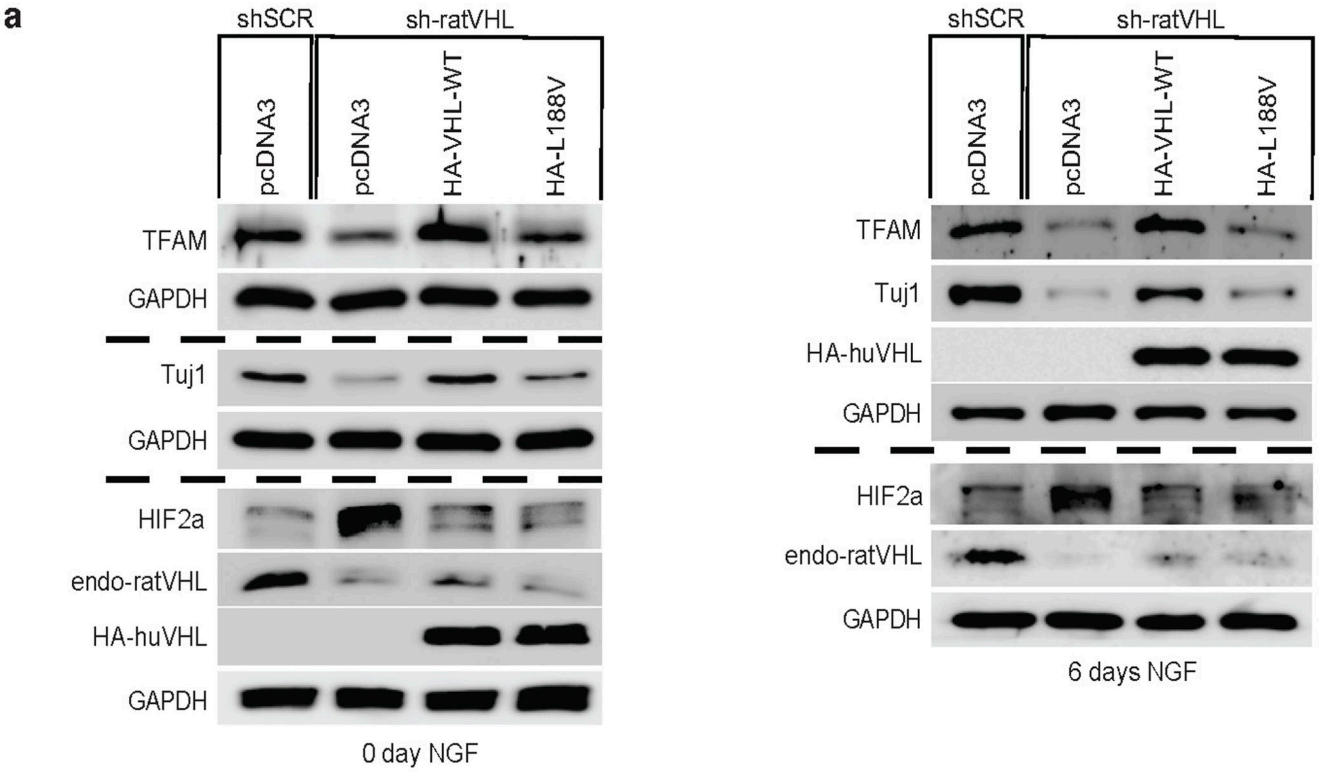

Extended Data Fig. 7. Low mitochondrial content in pheochromocytoma cells causes impaired differentiation.

(a) Immunoblot analysis of stable polyclonal PC12 cells expressing the indicated human VHL (huVHL) species. Stable polyclonal PC12 cells were transduced for 48 h with lentivirus encoding shRNA targeting endogenous rat VHL (endg. sh-ratVHL) or scramble control (shSCR) and subsequently treated with NGF for 6 days. n = 3 biological independent experiments.

Supplementary Material

Refer to Web version on PubMed Central for supplementary material.

Acknowledgments

Funding

W.L. was funded by the China Scholarship Council, S.L. and M.P. was funded by Swedish Childhood Cancer Fund. J.H. was funded by The Swedish Cancer Society, The Swedish Brain Foundation, Knut and Alice Wallenberg Foundation and L. Sagens and C. Erikssons Foundation. J.R. was funded by funding from the Swedish Research Council. A.vK. was funded by Multiuser Equipment Grant (208402/Z/17/Z) from the Wellcome trust. S.S. was funded by the Swedish Research Council, Swedish Childhood Cancer Fund, the Swedish Cancer Society, Knut and Alice Wallenberg Foundation and ParaDiff foundation and supported by ERC Synergy grant (KILL-OR-DIFFERENTIAT). The virus was made by VirusTech Core Facility of Karolinska Institutet.

Data availability

All data associated with this study are presented in the paper or the extended data figures. Source data are provided with this paper. Raw and analyzed mass spectrometry data are made available at http://www.ebi.ac.uk/pride.

References

1. Maxwell PH, et al. The tumour suppressor protein VHL targets hypoxia-inducible factors for oxygen-dependent proteolysis. Nature. 1999; 399: 271–275. DOI: 10.1038/20459 [PubMed: 10353251]
2. Kaelin WG Jr. The von Hippel–Lindau tumour suppressor protein: O2 sensing and cancer. Nature Reviews Cancer. 2008; 8: 865–873. DOI: 10.1038/nrc2502 [PubMed: 18923434]
3. Kaelin WG Jr, Ratcliffe PJ. Oxygen sensing by metazoans: the central role of the HIF hydroxylase pathway. Mol Cell. 2008; 30: 393–402. DOI: 10.1016/j.molcel.2008.04.009 [PubMed: 18498744]
4. Zhang H, et al. HIF-1 inhibits mitochondrial biogenesis and cellular respiration in VHL-deficient renal cell carcinoma by repression of C-MYC activity. Cancer Cell. 2007; 11: 407–420. DOI: 10.1016/j.ccr.2007.04.001 [PubMed: 17482131]
5. Kaelin WG Jr. The von Hippel-Lindau tumour suppressor protein: O2 sensing and cancer. Nature reviews. 2008; 8: 865–873.
6. Zhuang Z, et al. Somatic HIF2A gain-of-function mutations in paraganglioma with polycythemia. N Engl J Med. 2012; 367: 922–930. DOI: 10.1056/NEJMoa1205119 [PubMed: 22931260]
7. Taieb D, et al. Somatic gain-of-function HIF2A mutations in sporadic central nervous system hemangioblastomas. J Neurooncol. 2016; 126: 473–481. DOI: 10.1007/s11060-015-1983-y [PubMed: 26514359]
8. Toledo RA, et al. In vivo and in vitro oncogenic effects of HIF2A mutations in pheochromocytomas and paragangliomas. Endocr Relat Cancer. 2013; 20: 349–359. DOI: 10.1530/ERC-13-0101 [PubMed: 23533246]
9. Hoffman MA, et al. von Hippel-Lindau protein mutants linked to type 2C VHL disease preserve the ability to downregulate HIF. Human molecular genetics. 2001; 10: 1019–1027. [PubMed: 11331612]
10. Clifford SC, et al. Contrasting effects on HIF-1alpha regulation by disease-causing pVHL mutations correlate with patterns of tumourigenesis in von Hippel-Lindau disease. Human molecular genetics. 2001; 10: 1029–1038. [PubMed: 11331613]
11. Kaelin WG Jr. The VHL Tumor Suppressor Gene: Insights into Oxygen Sensing and Cancer. Trans Am Clin Climatol Assoc. 2017; 128: 298–307. [PubMed: 28790514]
12. Kurban G, et al. Collagen matrix assembly is driven by the interaction of von Hippel-Lindau tumor suppressor protein with hydroxylated collagen IV alpha 2. Oncogene. 2008; 27: 1004–1012. DOI: 10.1038/sj.onc.1210709 [PubMed: 17700531]
13. Grosfeld A, et al. Interaction of hydroxylated collagen IV with the von hippel-lindau tumor suppressor. J Biol Chem. 2007; 282: 13264–13269. DOI: 10.1074/jbc.M611648200 [PubMed: 17339318]

14. Ohh M, et al. The von Hippel-Lindau tumor suppressor protein is required for proper assembly of an extracellular fibronectin matrix. Mol Cell. 1998; 1: 959–968. S1097-2765(00)80096-9 [PubMed: 9651579]
15. Okuda H, et al. Direct interaction of the beta-domain of VHL tumor suppressor protein with the regulatory domain of atypical PKC isotypes. Biochem Biophys Res Commun. 1999; 263: 491–497. DOI: 10.1006/bbrc.1999.1347 [PubMed: 10491320]
16. Guo J, et al. pVHL suppresses kinase activity of Akt in a proline-hydroxylation-dependent manner. Science. 2016; 353: 929–932. DOI: 10.1126/science.aad5755 [PubMed: 27563096]
17. Liu X, et al. Genome-wide Screening Identifies SFMBT1 as an Oncogenic Driver in Cancer with VHL Loss. Mol Cell. 2020; 77: 1294–1306. e1295 doi: 10.1016/j.molcel.2020.01.009 [PubMed: 32023483]
18. Hu L, et al. TBK1 Is a Synthetic Lethal Target in Cancer with VHL Loss. Cancer Discov. 2020; 10: 460–475. DOI: 10.1158/2159-8290.CD-19-0837 [PubMed: 31810986]
19. Zhang J, et al. VHL substrate transcription factor ZHX2 as an oncogenic driver in clear cell renal cell carcinoma. Science. 2018; 361: 290–295. DOI: 10.1126/science.aap8411 [PubMed: 30026228]
20. Li S, et al. EglN3 hydroxylase stabilizes BIM-EL linking VHL type 2C mutations to pheochromocytoma pathogenesis and chemotherapy resistance. Proceedings of the National Academy of Sciences of the United States of America. 2019; 116: 16997–17006. DOI: 10.1073/pnas.1900748116 [PubMed: 31375625]
21. Ang SO, et al. Disruption of oxygen homeostasis underlies congenital Chuvash polycythemia. Nat Genet. 2002; 32: 614–621. DOI: 10.1038/ng1019 [PubMed: 12415268]
22. Gordeuk VR, et al. Congenital disorder of oxygen sensing: association of the homozygous Chuvash polycythemia VHL mutation with thrombosis and vascular abnormalities but not tumors. Blood. 2004; 103: 3924–3932. DOI: 10.1182/blood-2003-07-2535 [PubMed: 14726398]
23. Hickey MM, Lam JC, Bezman NA, Rathmell WK, Simon MC. von Hippel-Lindau mutation in mice recapitulates Chuvash polycythemia via hypoxia-inducible factor-2alpha signaling and splenic erythropoiesis. J Clin Invest. 2007; 117: 3879–3889. DOI: 10.1172/JCI32614 [PubMed: 17992257]
24. Bond J, et al. Dysregulation of the HIF pathway due to VHL mutation causing severe erythrocytosis and pulmonary arterial hypertension. Blood. 2011; 117: 3699–3701. DOI: 10.1182/blood-2010-12-327569 [PubMed: 21454469]
25. Liang H, Ward WF. PGC-1alpha: a key regulator of energy metabolism. Adv Physiol Educ. 2006; 30: 145–151. DOI: 10.1152/advan.00052.2006 [PubMed: 17108241]
26. Nilsson H, et al. Primary clear cell renal carcinoma cells display minimal mitochondrial respiratory capacity resulting in pronounced sensitivity to glycolytic inhibition by 3-Bromopyruvate. Cell Death Dis. 2015; 6 e1585 doi: 10.1038/cddis.2014.545 [PubMed: 25569102]
27. Xie L, et al. Oxygen-regulated beta(2)-adrenergic receptor hydroxylation by EGLN3 and ubiquitylation by pVHL. Science signaling. 2009; 2 ra33 doi: 10.1126/scisignal.2000444 [PubMed: 19584355]
28. Handschin C, Spiegelman BM. The role of exercise and PGC1alpha in inflammation and chronic disease. Nature. 2008; 454: 463–469. DOI: 10.1038/nature07206 [PubMed: 18650917]
29. Hillen HS, Morozov YI, Sarfallah A, Temiakov D, Cramer P. Structural Basis of Mitochondrial Transcription Initiation. Cell. 2017; 171: 1072–1081. e1010 doi: 10.1016/j.cell.2017.10.036 [PubMed: 29149603]
30. Shiao YH, Resau JH, Nagashima K, Anderson LM, Ramakrishna G. The von Hippel-Lindau tumor suppressor targets to mitochondria. Cancer Res. 2000; 60: 2816–2819. [PubMed: 10850420]
31. Lu B, et al. Phosphorylation of human TFAM in mitochondria impairs DNA binding and promotes degradation by the AAA+ Lon protease. Mol Cell. 2013; 49: 121–132. DOI: 10.1016/j.molcel.2012.10.023 [PubMed: 23201127]
32. Matsushima Y, Goto Y, Kaguni LS. Mitochondrial Lon protease regulates mitochondrial DNA copy number and transcription by selective degradation of mitochondrial transcription factor A (TFAM). Proc Natl Acad Sci U S A. 2010; 107: 18410–18415. DOI: 10.1073/pnas.1008924107 [PubMed: 20930118]

33. Couve S, et al. Genetic evidence of a precisely tuned dysregulation in the hypoxia signaling pathway during oncogenesis. Cancer Res. 2014; 74: 6554–6564. DOI: 10.1158/0008-5472.CAN-14-1161 [PubMed: 25371412]
34. Agathocleous M, et al. Metabolic differentiation in the embryonic retina. Nat Cell Biol. 2012; 14: 859–864. DOI: 10.1038/ncb2531 [PubMed: 22750943]
35. Zheng X, et al. Metabolic reprogramming during neuronal differentiation from aerobic glycolysis to neuronal oxidative phosphorylation. Elife. 2016; 5 doi: 10.7554/eLife.13374
36. Greene LA, Tischler AS. Establishment of a noradrenergic clonal line of rat adrenal pheochromocytoma cells which respond to nerve growth factor. Proceedings of the National Academy of Sciences of the United States of America. 1976; 73: 2424–2428. DOI: 10.1073/pnas.73.7.2424 [PubMed: 1065897]
37. Greene LA. Nerve growth factor prevents the death and stimulates the neuronal differentiation of clonal PC12 pheochromocytoma cells in serum-free medium. J Cell Biol. 1978; 78: 747–755. DOI: 10.1083/jcb.78.3.747 [PubMed: 701359]
38. Barletta JA, Hornick JL. Succinate dehydrogenase-deficient tumors: diagnostic advances and clinical implications. Adv Anat Pathol. 2012; 19: 193–203. DOI: 10.1097/PAP.0b013e31825c6bc6 [PubMed: 22692282]
39. Toro JR, et al. Mutations in the fumarate hydratase gene cause hereditary leiomyomatosis and renal cell cancer in families in North America. Am J Hum Genet. 2003; 73: 95–106. DOI: 10.1086/376435 [PubMed: 12772087]
40. Ward PS, et al. The common feature of leukemia-associated IDH1 and IDH2 mutations is a neomorphic enzyme activity converting alpha-ketoglutarate to 2-hydroxyglutarate. Cancer Cell. 2010; 17: 225–234. DOI: 10.1016/j.ccr.2010.01.020 [PubMed: 20171147]
41. Wang Y, et al. WT1 recruits TET2 to regulate its target gene expression and suppress leukemia cell proliferation. Mol Cell. 2015; 57: 662–673. DOI: 10.1016/j.molcel.2014.12.023 [PubMed: 25601757]
42. Kaelin WG. Von Hippel-Lindau disease. Annu Rev Pathol. 2007; 2: 145–173. DOI: 10.1146/annurev.pathol.2.010506.092049 [PubMed: 18039096]
43. Brauch H, et al. Sporadic pheochromocytomas are rarely associated with germline mutations in the vhl tumor suppressor gene or the ret protooncogene. J Clin Endocrinol Metab. 1997; 82: 4101–4104. DOI: 10.1210/jcem.82.12.4454 [PubMed: 9398721]
44. Percy MJ, et al. A gain-of-function mutation in the HIF2A gene in familial erythrocytosis. N Engl J Med. 2008; 358: 162–168. DOI: 10.1056/NEJMoa073123 [PubMed: 18184961]
45. Chen W, et al. Targeting renal cell carcinoma with a HIF-2 antagonist. Nature. 2016; 539: 112–117. DOI: 10.1038/nature19796 [PubMed: 27595394]
46. Vander Heiden MG, DeBerardinis RJ. Understanding the Intersections between Metabolism and Cancer Biology. Cell. 2017; 168: 657–669. DOI: 10.1016/j.cell.2016.12.039 [PubMed: 28187287]
47. Siegel RL, Miller KD, Jemal A. Cancer Statistics, 2017. CA Cancer J Clin. 2017; 67: 7–30. DOI: 10.3322/caac.21387 [PubMed: 28055103]
48. Schlisio S, et al. The kinesin KIF1Bbeta acts downstream from EglN3 to induce apoptosis and is a potential 1p36 tumor suppressor. Genes & development. 2008; 22: 884–893. [PubMed: 18334619]
49. Young AP, et al. VHL loss actuates a HIF-independent senescence programme mediated by Rb and p400. Nature cell biology. 2008; 10: 361–369. [PubMed: 18297059]
50. Fell SM, et al. Neuroblast differentiation during development and in neuroblastoma requires KIF1Bbeta-mediated transport of TRKA. Genes & development. 2017; 31: 1036–1053. DOI: 10.1101/gad.297077.117 [PubMed: 28637693]
51. Welander J, et al. Rare germline mutations identified by targeted next-generation sequencing of susceptibility genes in pheochromocytoma and paraganglioma. J Clin Endocrinol Metab. 2014; jc20134375 doi: 10.1210/jc.2013-4375
52. Li S, et al. The 1p36 Tumor Suppressor KIF 1Bbeta Is Required for Calcineurin Activation, Controlling Mitochondrial Fission and Apoptosis. Dev Cell. 36: 164–178. DOI: 10.1016/j.devcel.2015.12.029
53. Rodriguez J, et al. Substrate-Trapped Interactors of PHD3 and FIH Cluster in Distinct Signaling Pathways. Cell Rep. 14: 2745–2760. DOI: 10.1016/j.celrep.2016.02.043

54. Lee S, et al. Neuronal apoptosis linked to EglN3 prolyl hydroxylase and familial pheochromocytoma genes: developmental culling and cancer. Cancer Cell. 2005; 8: 155–167. [PubMed: 16098468]
55. Minczuk M, et al. TEFM (c17orf42) is necessary for transcription of human mtDNA. Nucleic Acids Res. 2011; 39: 4284–4299. DOI: 10.1093/nar/gkq1224 [PubMed: 21278163]

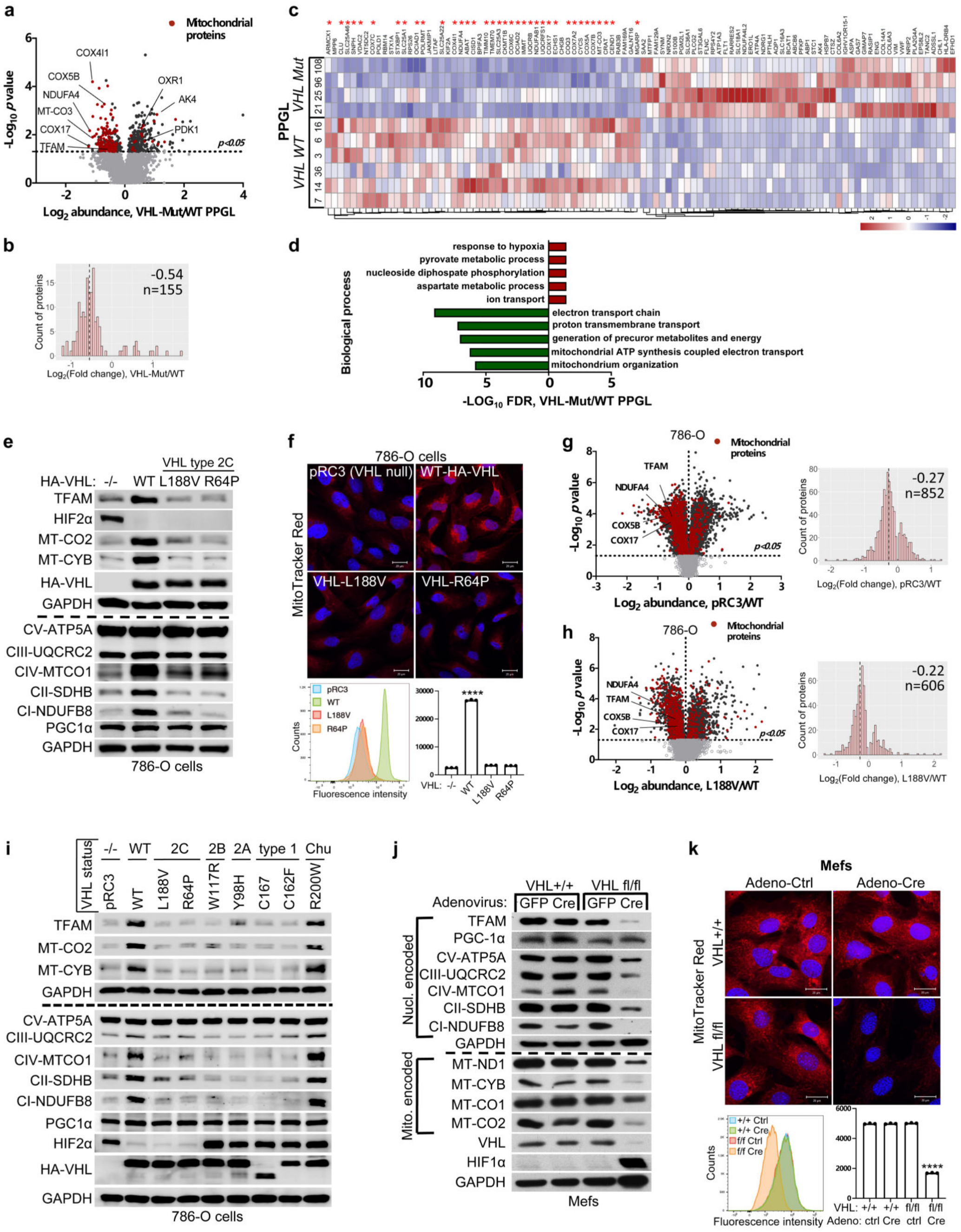

Figure 1. pVHL regulates of mitochondrial mass independent of HIFα.

a, Volcano plot of proteins detected by nanoLC-MS/MS in human PPGL tumors. (*VHL* mutant/ wild-type). Line indicates a p-value of 0.05 (-Log_{10} p value= 1.3) in two-tailed unpaired t-test. **b,** Histogram of mitochondrial proteins regulated in human VHL mutant compared to *VHL* wild-type PPGL tumors. **c,** Heatmap of top 50 down- and up- regulated proteins in human VHL related PPGL tumors (VHL mutant/ wild-type). Red stars indicate mitochondrial proteins. **d,** Top 5 biological processes of top 50 up (red)- and down (green)-regulated proteins for human VHL PPGL tumors. **e,** Immunoblot of 786-O cells stably expressing wildtype pVHL (WT) or type 2C pVHL mutants (L188V or R64P). n = 3 biological independent experiments. The corresponding immunofluorescence images is shown in **f**. Top: Cells were stained by MitoTracker Red. Bottom: Flow cytometry analysis of MitoTracker Green-stained cells. Data are presented as mean values ± SD. One way ANOVA Tukey's Multiple Comparison Test. ****p <0.0001. n = 3 biological independent experiments. **g,** Left: Volcano plot of proteins detected by nanoLC-MS/MS in human ccRCC cells (786-O). *VHL*-null cells (pRC3) were compared to *VHL* wild-type (WT) expressing cells. Line indicates a p-value of 0.05 (-Log10 p value= 1.3) in two-tailed unpaired t-test. Right: Histogram of fold changes of mitochondrial proteins comparing pRC3 to *VHL*-WT with indicted median value of Log2(Fold change) -0.27. **h,** Left: Volcano plot of proteins detected by nanoLC-MS/MS in 786-O cells. *VHL*-L188V mutant cells were compared to *VHL* wild-type expressing cells as in (G). Right: Histogram of fold changes of mitochondrial proteins comparing *VHL*-L188V to *VHL*-WT with indicated median value of Log2(Fold change) of -0.22. **i,** Immunoblot of 786-O cells stably transfected to produce the indicated pVHL species. **j,** Immunoblot of *VHL* MEFs with indicated genotype. i,j, n = 3 biological independent experiments. The corresponding immunofluorescence of *VHL* MEFs is shown in **k.** Top: Cells were stained by MitoTracker Red to visualize mitochondria. Bottom: Flow cytometry analysis of MitoTraker Green-stained MEFs. n = 3 biological independent experiments. Data are presented as mean values ± SD. One way ANOVA Tukey's Multiple Comparison Test. ****p <0.0001

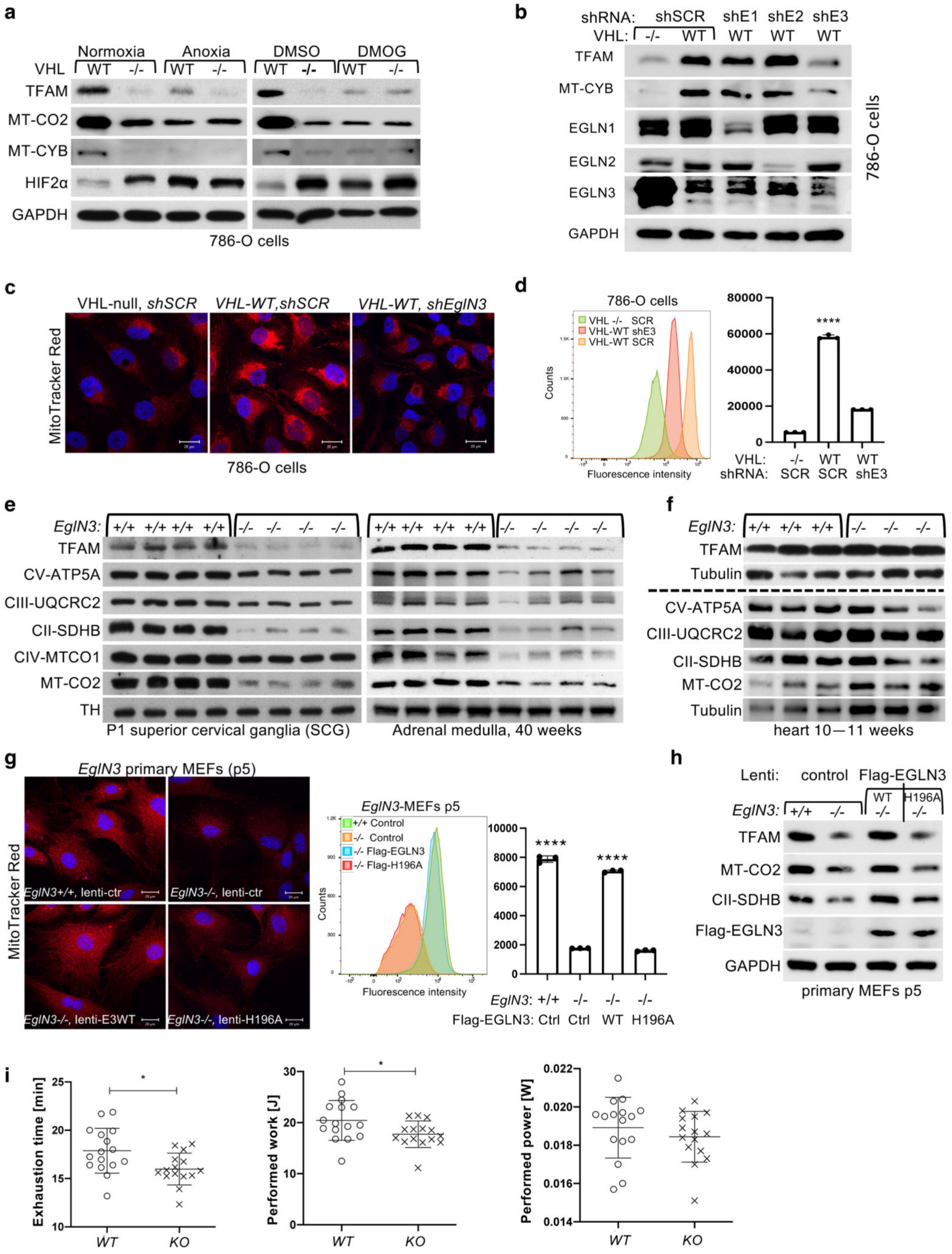

Figure 2. pVHL regulation of mitochondrial mass is hydroxylation and EGLN3 dependent.

a, Immunoblot analysis of 786-O cells with indicated genotype upon anoxic condition for 16 h or treated with 1 mM DMOG for 8 h. n = 3 biological independent experiments. **b,** Immunoblot analysis of 786-O cells with indicated VHL status transduced with lentiviral pL.KO shRNA targeting *EGLN1* (shE1), *EGLN2* (shE2), *EGLN3* (shE3) or no targeting control (shSCR). n = 3 biological independent experiments. **c,** Fluorescence images of 786-O cells with indicated VHL status transduced with lentiviral pL.KO shRNA targeting *EGLN3* or no targeting control. Mitochondria are visualized by MitoTracker Red staining.

Corresponding flow cytometry analysis of MitoTracker Green-stained 786-O cells is shown in **d**. Data are presented as mean values ± SD. One way ANOVA Tukey's Multiple Comparison Test. ****p <0.0001. n = 3 biological independent experiments. **e,** Immunoblot analysis of mouse superior cervical ganglia (SCG) (left), adrenal gland medulla (right) of indicated genotype. n = 4 biologically independent *EGLN3* wildtype or knockout mice. **f,** Immunoblot analysis of mouse heart of indicated genotype. n=3 biologically independent *EGLN3* wildtype or knockout mice. **g,** Left: Fluorescence images of primary *EGLN3* MEFs of indicated genotype stably transduced with lentivirus encoding *EGLN3* WT, catalytic death mutant *EGLN3*-H196A or empty control. Mitochondria are visualized by MitoTracker Red staining. Right: Corresponding flow cytometry analysis of MitoTracker Green-stained primary MEFs cells of indicated genotype stably transduced with lentivirus encoding *EGLN3* WT, catalytic death mutant *EGLN3*-H196A or empty control. n = 3 biological independent experiments. Data are presented as mean values ± SD. One way ANOVA Tukey's Multiple Comparison Test. ****p <0.0001. Corresponding immunoblot of primary *EGLN3* MEFs is shown in **h**. n = 3 biological independent experiments. **i,** Aged, 56-60 weeks old KO mice reach exhaustion significantly earlier and perform less work at comparable performed power (WT n=16, KO n=15 independent biological samples per genotype, male mice). Data are presented as mean values ± SD. Two-tailed unpaired t test. p =0.014, p =0.0318.

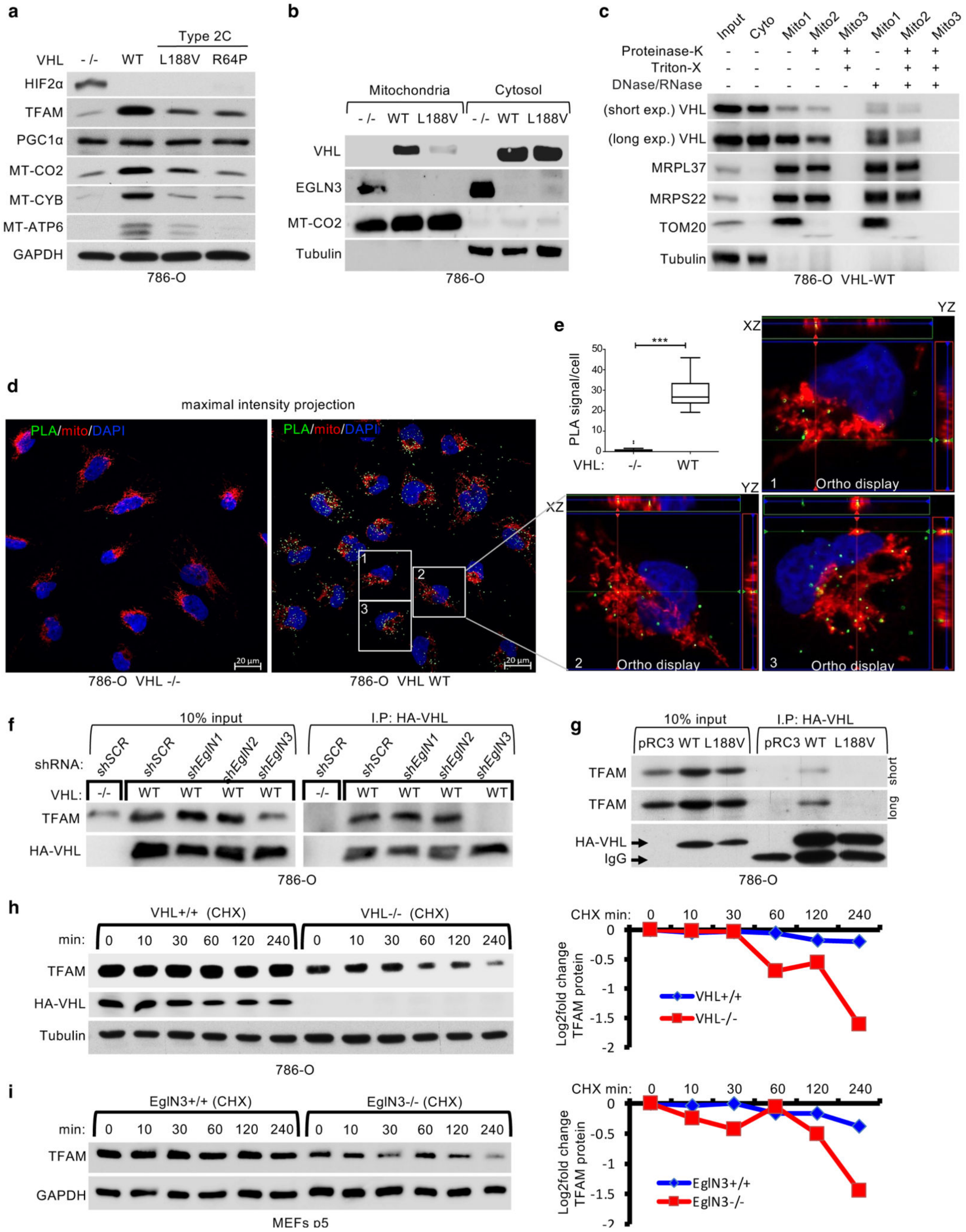

Figure 3. pVHL regulates TFAM protein stability depending on EGLN3 enzymatic activity.

a, Immunoblot of 786-O cells stably transfected to produce the indicated pVHL species. **b,** Immunoblot analysis of mitochondrial and cytosolic fractions of 786-O stable cells. **c,** Immunoblot analysis of subcellular fractionation of 786-O pVHL wild-type (WT) cells. Mitochondrial fractions were treated with 25 μg/ml Proteinase K with or without 1% Triton X-100. a-c, n = 3 biological independent experiments. **d,** Representative confocal images of in situ proximity ligation assay (PLA) between TFAM and pVHL in 786-O cells with indicated *VHL* status. PLA signal is shown in green, DAPI (blue) and MitoTracker

Red (red) in maximal intensity projection. Orthogonal view of three cells identified in pVHL expressing cells are presented and demonstrate co-localization of PLA signal in mitochondria (yellow). Magnification 63x; scale bar: 5 µm. **e,** Quantification of the number of PLA signals per cell in both conditions with indicated *VHL* status; Mann-Whitney U test; *** P value <0.001. (n >200 cells per group examined). Similar results were seen more than three times. The term five-number summary is used to describe a list of five values: the minimum, the 25th percentile, the median, the 75th percentile, and the maximum. These are the same values plotted in a box-and-whiskers plot when the whiskers extend to the minimum and maximum. **f,** Immunoblots of HA-VHL immunoprecipitation from 786-O cells transduced with lentivirus encoding shRNA targeting *EGLN1*, *EGLN2*, *EGLN3* or scramble control (SCR). **g,** HA-VHL immunoprecipitation from 786-O cells with stable expression of either HA-VHL wild-type (WT) or HA-VHL-L188V. Immunoblots showing co-immunoprecipitation of endogenous TFAM and HA-VHL. **h,** Left: 786-O *VHL*-null cells (-/-) or stable HA-VHL wild-type (WT) expressing cells were treated with 10 µg/ml cycloheximide (CHX). At the indicated time points, whole-cell lysates were prepared for immunoblot analysis. Right: Corresponding quantification of the band intensities. **i,** Left: *EGLN3* MEFs with indicated genotype were treated with cycloheximide (CHX) at the concentration of 10 µg/ml and whole-cell lysates were prepared for immunoblot analysis at the indicated time points. Right: Corresponding quantification of the band intensities. f-i, n = 3 biological independent experiments.

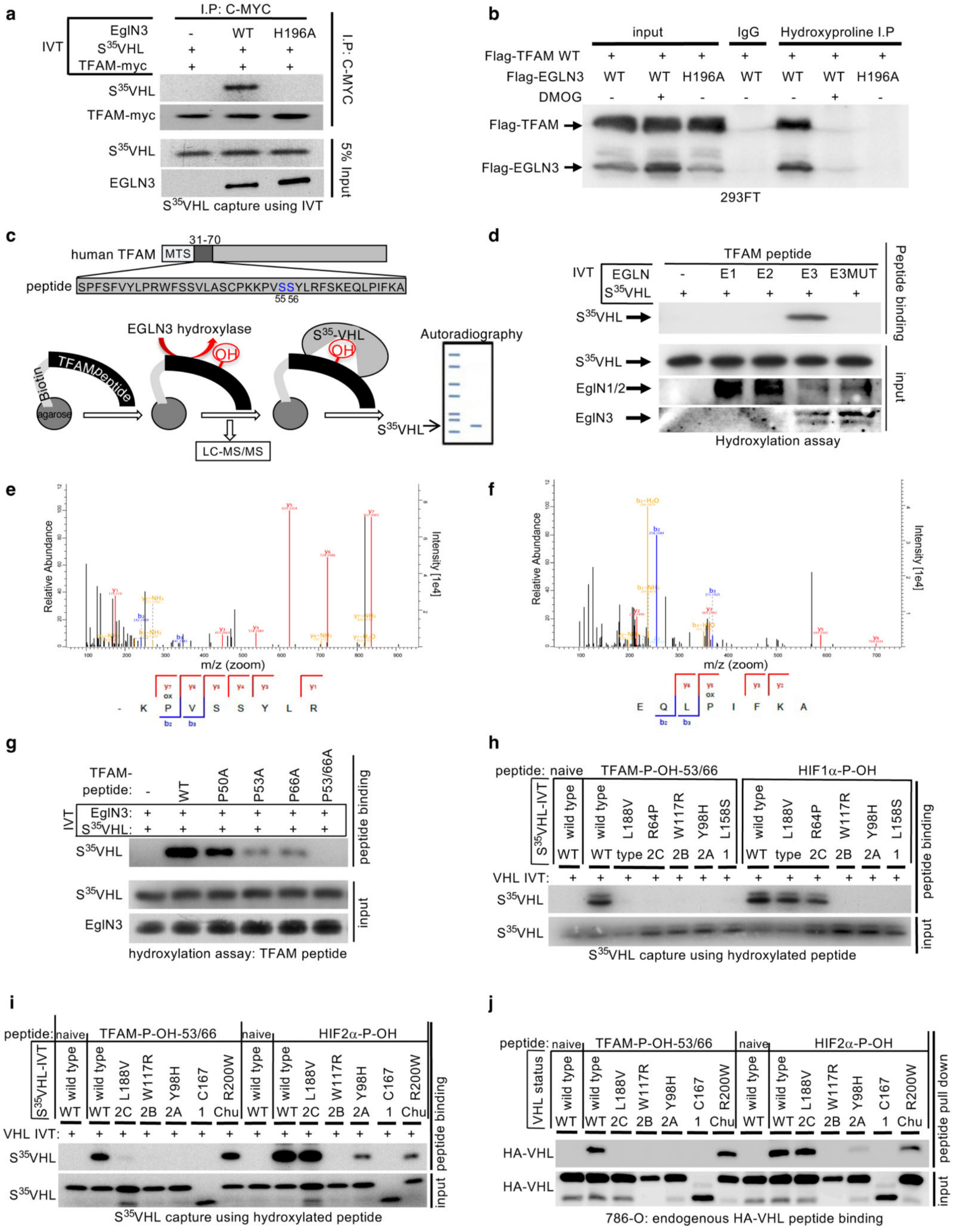

Figure 4. TFAM is hydroxylated by EGLN3 at Proline 53/66 causing pVHL recognition.

a, Autoradiograms showing recovery of ^{35}S-labeled VHL protein bound to HA-immunoprecipitated full length TFAM that was first subjected before to hydroxylation by EGLN3 wild-type (WT) or EGLN3-H196A catalytic mutant. **b,** Immunoprecipitation using antihydroxyproline antibody (HydroxyP) from 293FT cells that were transiently transfected with plasmids encoding Flag-TFAM and Flag-EGLN3 WT or catalytic-dead mutant (H196A) with or without DMOG treatment. Immunoblots show coimmunoprecipitation of Flag-TFAM and Flag-EGLN3. a,b, n = 3 biological independent experiments. **c,**

Schematic representation of the hydroxylation assay using the biotinylated synthetic TFAM peptide-31-70. **d,** Autoradiograms showing recovery of ^{35}S-labeled VHL protein bound to biotinylated TFAM-peptide-31-70. Prior to pull-down, peptides were incubated with either EGLN1, EGLN2, EGLN3 or EGLN3 catalytic mutant (Mut) generated by IVT or unprogrammed reticulocyte lysate (-). Expression of IVT-produced EglN proteins in each reaction was verified by immunoblot. n = 3 biological independent experiments. **e-f,** Mass spectrometry of biotinylated TFAM-peptide-30-70 subjected to EGLN3 hydroxylation assay. Representative fragmentation spectra of hydroxylated Biotin-KP(ox)VSSYLR (**e**) and hydroxylated Biotin-EQLP(ox)IFKA (**f**). **g,** Autoradiograms of EGLN3 hydroxylation and ^{35}S-VHL capture as shown in using biotinylated TFAM peptides containing proline to alanine substitutions, or no substitution (WT). **h,** Autoradiograms showing recovery of 35S-labeled VHL protein (WT) or corresponding disease mutants (as indicated) bound to biotinylated TFAM-peptides synthesized with double hydroxyl-prolines on prolines 53 and 66 (TFAM-P-OH-53/66). Synthetic biotinylated HIF1α peptide (residues 556 to 575) with hydroxylated proline 564 (HIF1α-P-OH) was included as a control. Biotinylated TFAM naïve peptide was used as negative controls. **i,** Autoradiograms showing recovery of 35S-labeled VHL protein (WT) or corresponding disease mutants (as indicated) bound to biotinylated TFAM-peptides synthesized with double hydroxyl-prolines on prolines 53 and 66 (TFAM-P-OH-53/66). Synthetic biotinylated HIF2α peptide (residues 521 to 543) with hydroxylated proline 531 (HIF2α-P-OH) was included as a control. Biotinylated TFAM and HIF2α naïve peptides were used as negative controls. **j,** Peptide pulldown using biotinylated TFAM-P-OH-53/66 peptide incubated with whole-cell lysates from 786-O cells expressing either HA-VHL WT or HA-VHL disease mutant. Biotinylated TFAM and HIF2α naïve peptides were used as negative controls. g-j, n = 3 biological independent experiments.

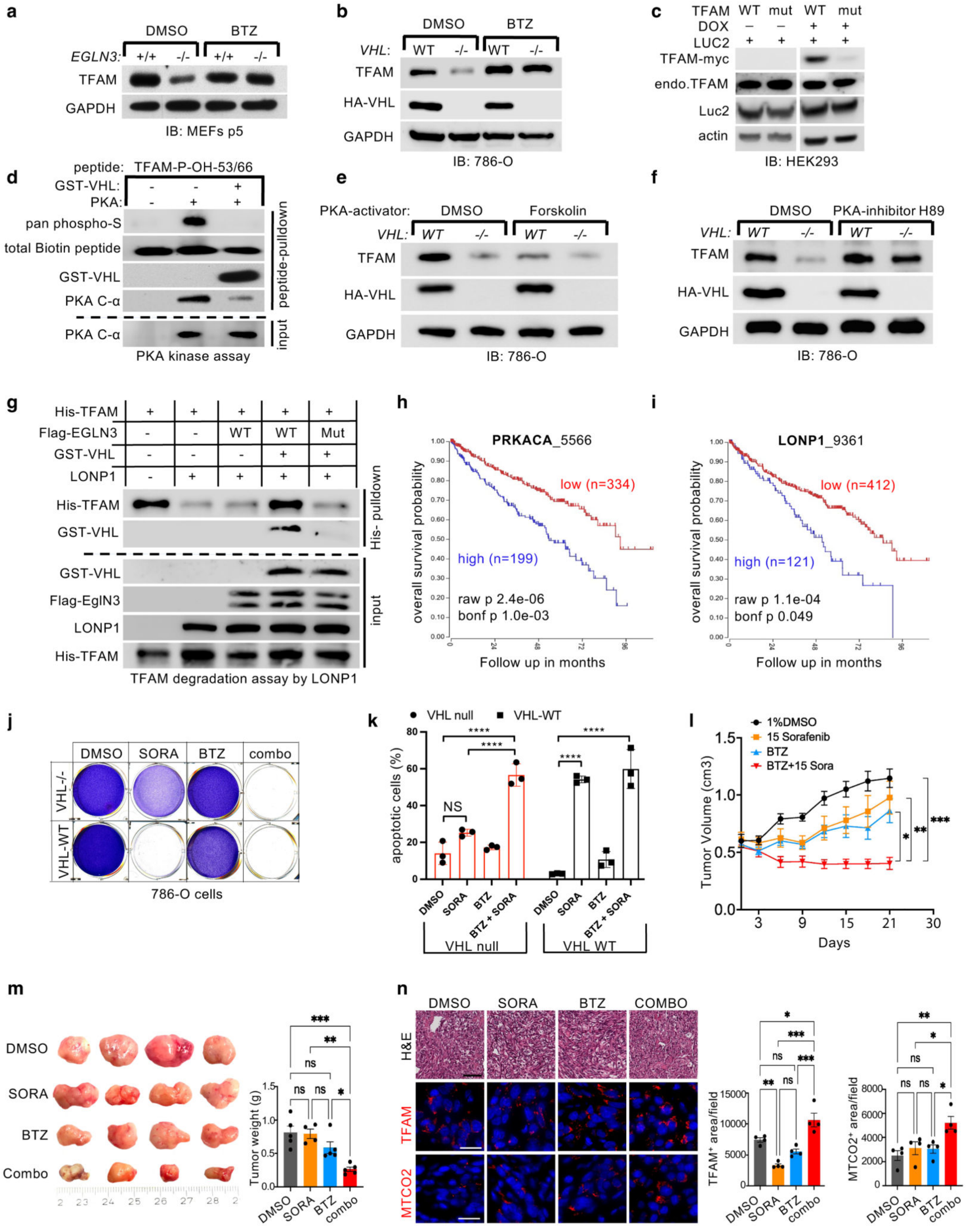

Figure 5. pVHL protects TFAM from LONP1 degradation.

a-b, Immunoblot analysis of primary *EglN3+/+* and *EglN3-/-* MEFs (a) and 786-O cells (b) treated with 1 µM LONP1 inhibitor Bortezomib (BTZ) for 16 hours. **c,** Immunoblot analysis of HEK293 cells transfected with Transposon vectors pB-TRE-TFAM-wt-Luc2, pB-TRE-TFAM-mut-Luc2 and transposase vector pCAGhypbase. **d,** Immunoblot analysis of PKA kinase activity assay using biotinylated TFAM-peptides with double hydroxyl-prolines 53 and 66. **e-f,** Immunoblot analysis of 786-O cells treated with 20 µM PKA activator Forskolin (24h) (e) or 5 µM PKA inhibitor H89 (24h) (f). **g,** Immunoblot analysis of TFAM degradation assay by LONP1 using purified His-TFAM, GST-VHL, LONP1 and IVT-synthesized Flag-EGLN3 wild-type or Flag-EGLN3 catalytic mutant. a-g, n = 3 biological independent experiments. **h-i,** Kaplan-Meier overall survival curve for individuals with high (blue) and low (red) expression of (h) Protein kinase A catalytic subunit (PRKACA) and (i) LONP1 using the Tumor Kidney Renal Clear Cell Carcinoma-TCGA-533 dataset(https://hgserver1.amc.nl/cgi-bin/r2/main.cgi) (minimal patient group size to 50 in the iterations). The overall survival probability was estimated with the KaplanScanner tool, using a Bonferroni-corrected logrank test between the two groups of patients. The graph depicts the best p-value corrected for multiple testing (Bonferroni correction). **j**, Crystal violet staining of 786-O cells pretreated with Bortezomib (BTZ; 10 nM) for 24 hours and then treated for 48 hours with sorafenib (SORA; 20 μM), Bortezomib (10 nM), or a combination (combo) of these 2 drugs as indicated. **k**, Cell apoptosis rate was detected by Annexin V-FITC/PI staining using flow cytometry. Data are presented as mean values ± SD. Two way ANOVA Tukey's Multiple Comparison Test. ****p <0.0001. n = 3 biological independent experiments. **l**, Female athymic NCr nu/nu mice were implanted subcutaneously with 786-O cells. Sorafenib (n=4) or vehicle control (DMSO, n=5) was administered orally, once a day at the dose of 15 mg/kg. Bortezomib (BTZ, n=5) was administered by intraperitoneal injection, twice per week at the dose of 1 mg/kg. Combined treatment: 1 mg/kg BTZ + 15 mg/kg sorafenib (n=5). Mean (±s.e.m.) tumor volume data are shown. *p <0.01, **p <0.01, ***p <0.001. **m**, Representative images of tumors after dissection and quantification of tumor weight of each treatment group as indicated. **n**, Representative hematoxylin and eosin (H&E, bar=50 um ×100), TFAM and MTCO2 immuno-fluorescence stainings (bar= 50 um ×400) of tumor tissues including quantification.

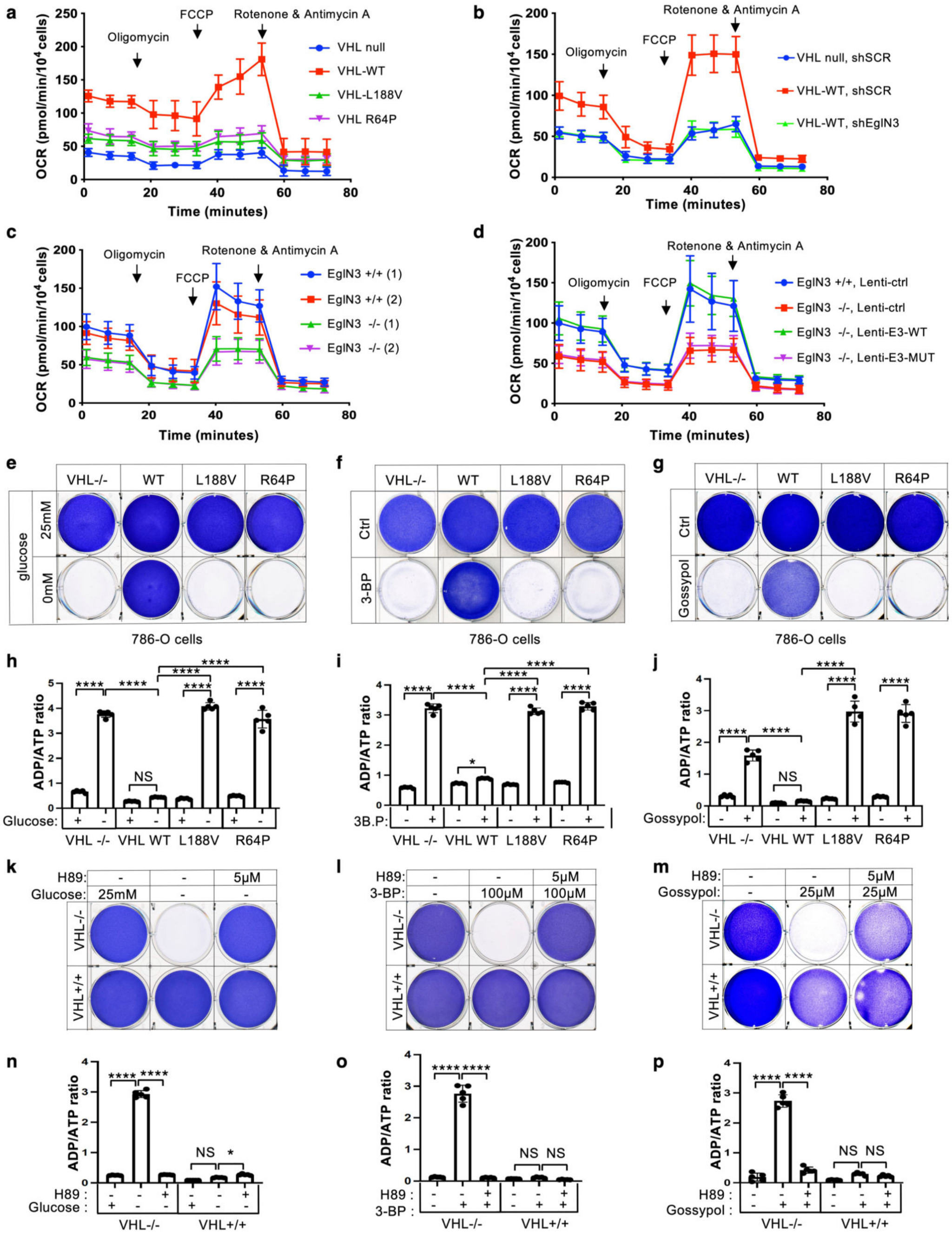

Figure 6. pVHL restores cellular oxygen consumption rate.

a, Mitochondrial respiration reflected by oxygen consumption rate (OCR) of 786-O cells with indicated genotype was monitored using the Seahorse XF-96 Extracellular Flux Analyzer with the sequential injection of oligomycin (1 μM), FCCP (1 μM), and rotenone/antimycin (0.5 μM). **b-c**, The measurement of oxygen consumption rate (OCR) of 786-O cells with indicated VHL status transduced with lentiviral pL.KO shRNA targeting *EGLN3* or no targeting control (b), primary *EGLN3+/+* and *EGLN3-/-* MEFs (c) stably transduced with lentivirus encoding EglN3 WT, catalytic death mutant or empty control (d). **a-d,** data are presented as mean values ± SD. n = 3 biological independent experiments. **e,** Crystal violet staining of 786-O cells with indicated VHL status treated with high glucose (25 mM) or no glucose (0 mM) respectively for 36 hours. Corresponding ADP/ATP ratio is shown in **(h)**. **f,** Crystal violet staining of 786-O cells with indicated VHL status treated with 100 μM 3-bromopyruvic acid (3-BP) for 4 hours. Corresponding ADP/ATP ratio is shown in **(i). g,** Crystal violet staining of 786-O cells with indicated VHL status treated with 25 μM gossypol for 36 hours. Corresponding ADP/ATP ratio is shown in (**j**). h-j, data are presented as mean values ± SD. One way ANOVA Tukey's Multiple Comparison Test. $^*p < 0.05$, $^{****}p < 0.0001$. n = 3 biological independent experiments. **k,** Crystal violet staining of 786-O cells with indicated VHL status treated with 5 μM PKA inhibitor H89 for 24 hours, prior to glucose deprivation for 36 hours. Corresponding ADP/ATP ratio is shown in **(n)**. **l,** Crystal violet staining of 786-O cells treated with 5 μM PKA inhibitor H89 for 24 hours, prior to 100 μM 3-BP treatment for 4 hours. Corresponding ADP/ATP ratio is shown in **(o)**. **m,** Crystal violet staining of 786-O cells treated with 5 μM PKA inhibitor H89 for 24 hours, prior to 25 μM gossypol for 36 hours. Corresponding ADP/ATP ratio is shown in **(p)**. n-p, data are presented as mean values ± SD. One way ANOVA Tukey's Multiple Comparison Test. $^*p < 0.05$, $^{****}p < 0.0001$. n = 3 biological independent experiments.

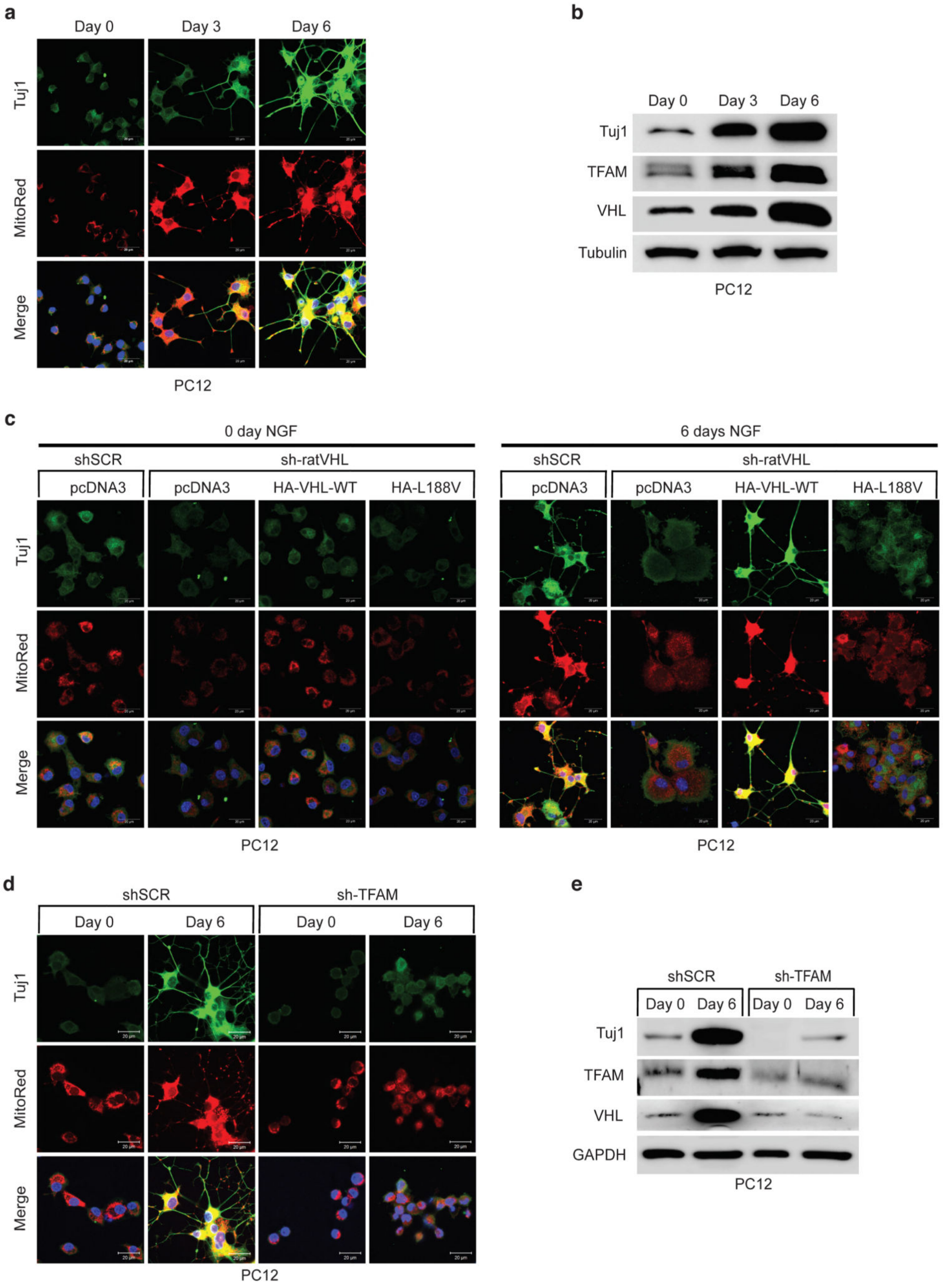

Figure 7. Low mitochondrial content in pheochromocytoma cells causes impaired differentiation.

a, Fluorescence images of PC12 cells treated with 50 ng/ml NGF with indicated time points. Cells were stained by MitoTracker Red to visualize mitochondria and endogenous Tuj1 (Neuron-specific class III beta-tubulin) was stained in green. Corresponding immunoblot analysis is shown in **b**. n = 3 biological independent experiments. **c**, Fluorescence images of stable polyclonal PC12 cells expressing the indicated human *VHL* (huVHL) species selected with G418 (0.5 mg/mL) for 2 weeks. PC12 clones were transduced for 48 h with lentivirus encoding shRNA targeting endogenous rat *VHL* (endg. sh-ratVHL) or scramble control (shSCR) and subsequently treated with NGF for 6 days. Cells were stained by MitoTracker Red to visualize mitochondria and endogenous Tuj1 was stained in green. **d**, Fluorescence images of polyclonal PC12 cells transduced for 48h with lentivirus encoding shRNA targeting endogenous rat *TFAM* (sh-TFAM) or scramble control (shSCR) and subsequently treated with NGF for 6 days. Cells were stained by MitoTracker Red to visualize mitochondria and endogenous Tuj1 in green. Corresponding immunoblot analysis is shown in **e**. n = 3 biological independent experiments. (a, c, d) Similar results were seen more than three times.

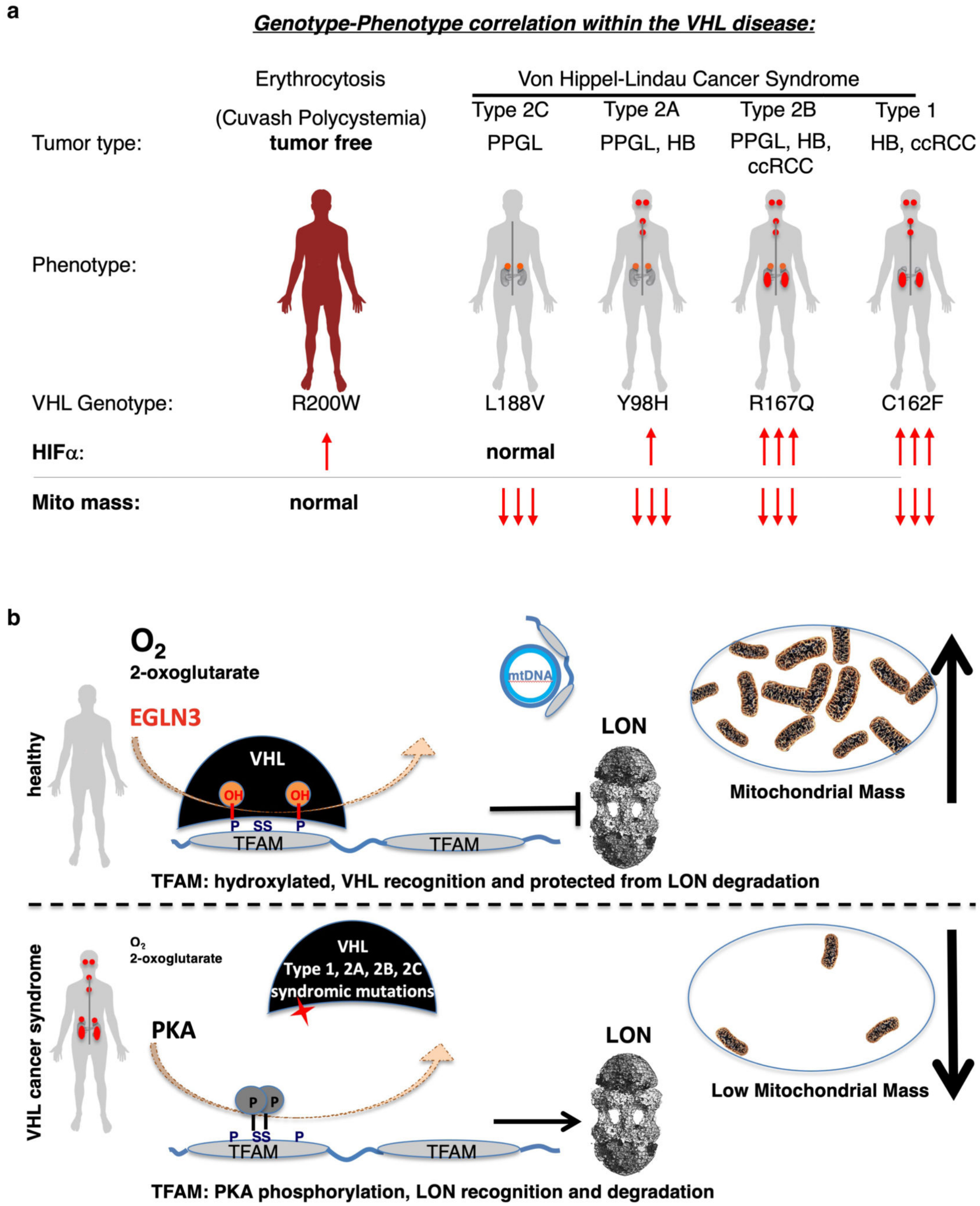

Figure 8. Schematic of oxygen dependent regulation of mitochondrial content within the von Hippel-Lindau (VHL) syndrome

a, Genotype-phenotype correlation in cancers arising in the VHL syndrome and its association with regulation of HIFα and mitochondrial content. Note: Cuvash polycythemia mutation VHL^{R200W} shows total absence of tumor development despite increased HIFα signaling and appears normal in regard of regulating mitochondrial content. **b**, Schematic representation of oxygen dependent regulation of mitochondrial transcription factor TFAM by pVHL, independent of the canonical substrate HIFα.